Electro-Optics Systems Laboratory
Department of Electrical and Computer Engineering

Rayleigh Lidar Observations of Gravity Wave Activity in the Stratosphere and Lower Mesosphere

M. S. Miller ▪ C. S. Gardner ▪ C. H. Liu
EOSL No. 87-008 ▪ December 1987

University of Illinois at Urbana-Champaign

UILU-ENG-87-2554

RAYLEIGH LIDAR OBSERVATIONS OF GRAVITY WAVE ACTIVITY IN THE STRATOSPHERE AND LOWER MESOSPHERE

by

M. S. Miller
C. S. Gardner
C. H. Liu

EOSL No. 87-008

Technical Report
December 1987

Supported by
Grant Nos.
NSF ATM86-10142
AFGL Subcontract on NASA NSG-5049

National Science Foundation
Air Force Geophysics Laboratory
National Aeronautics & Space Administration

ELECTRO-OPTIC SYSTEMS LABORATORY
DEPARTMENT OF ELECTRICAL AND COMPUTER ENGINEERING
COLLEGE OF ENGINEERING
UNIVERSITY OF ILLINOIS
URBANA, ILLINOIS 61801

ABSTRACT

Forty-two monochromatic gravity wave events were observed in the 25-55 km altitude region during 16 nights of Rayleigh lidar measurements at Poker Flat, Alaska, and Urbana, Illinois. The measured wave parameters were compared to previous radar and lidar measurements of gravity wave activity. Vertical wavelengths (λ_z) between 2 and 11.5 km with vertical phase velocities (c_z) between 0.1 and 1 m/s were observed. Measured values of λ_z and c_z were used to infer observed wave periods (T_{ob}) between 50 and 1000 minutes and horizontal wavelengths (λ_x) from 25 to 2000 km. Dominant wave activity was found at vertical wavelengths between 2-4 km and 7-10 km. No seasonal variations were evident in the observed wave parameters. Vertical and horizontal wavelengths showed a clear tendency to increase with T_{ob}, which is consistent with recent sodium lidar studies of monochromatic wave events near the mesopause. Measured power law relationships between the wave parameters were $\lambda_z \propto T_{ob}^{0.96}$, $\lambda_x \propto T_{ob}^{1.8}$ and $c_z \propto T_{ob}^{-0.85}$. The kinetic energy calculated for the monochromatic wave events varied as k_z^{-2}, k_x^{-1}, and $f_{ob}^{-1.7}$. The atmospheric scale heights calculated for each observation date ranged from 6.5 to 7.6 km with a mean value of 7 km. The increase of rms wind perturbations with altitude indicated an amplitude growth length of 20.9 km. The altitude profile of kinetic energy density decreased with height, suggesting that waves in this altitude region were subject to dissipation or saturation effects.

TABLE OF CONTENTS

1. INTRODUCTION

The study of atmospheric gravity waves is essential to understanding the large-scale circulation and dynamic structure of the middle atmosphere. Observational studies of gravity wave activity have focused on measurements of monochromatic wave parameters and characterization of the continuous gravity wave spectra in order to quantify gravity wave saturation effects and identify gravity wave variability with altitude, season and location [Fritts, 1984]. Analyses of the temporal frequency and wavenumber spectra of atmospheric wind fluctuations suggest the existence of an invariant spectral shape, which is predicted as a consequence of the saturation of vertically propagating gravity waves [Dewan and Good, 1986; Smith et al., 1987].

Radar and lidar are the predominant remote sensing techniques used to study gravity waves in the middle atmosphere. Radar has been successfully used to measure the vertical wavenumber and temporal frequency spectra of gravity wave activity [Smith et al., 1985; Balsley and Carter, 1982]. Statistical studies of the variability of gravity wave motions as a function of altitude and time have been accomplished in the 60-110 km altitude region using MF radar [Vincent and Fritts, 1987]. Monochromatic wave events have been observed and characterized with MF radar in the same altitude region, using three receiving antennas to measure horizontal wavelengths and phase speeds [Meek et al., 1985]. However, monochromatic wave activity is less prevalent in radar data than in lidar profiles, and consequently, the most extensive statistical studies of monochromatic gravity wave events have been conducted with lidar.

The feasibility of studying atmospheric dynamics with lidar techniques based on resonant backscatter from sodium atoms and Rayleigh backscatter from the atmosphere is well established. Lidar studies of gravity wave activity generally concentrate on observations of monochromatic events, since wave perturbations usually appear as individual events in lidar profiles. The University of Illinois at Urbana-Champaign (UIUC) sodium lidar has been used to observe the spatial and temporal variations in the sodium layer at the 80-105 km altitude region and study the propagation of gravity waves near the mesopause [Rowlett et al., 1978; Richter et al., 1981; Shelton et al., 1980; Gardner et al., 1986]. The parameters of monochromatic gravity waves can be extracted from sodium profiles [Gardner and Shelton, 1985] and used to infer wave saturation and dissipation effects [Gardner and Voelz, 1985]. An extensive characterization of monochromatic gravity wave events appearing in the sodium layer above Urbana, IL has been recently published [Gardner and Voelz, 1987].

The altitude region from 25-60 km is generally inaccessible with existing MST radar and has not been extensively studied. The lack of observational data in this region provides the scientific motivation for Rayleigh lidar studies of atmospheric dynamics. The observation altitudes for Rayleigh scatter are not limited to regions containing specific atmospheric

constituents, as with sodium lidar and other resonance fluorescence lidar techniques. Rayleigh lidar is limited only by the presence of aerosols in the atmosphere and by system noise. Rayleigh lidar systems have been successfully used to measure atmospheric density and temperature in the 30-80 km altitude region as well as to study gravity wave activity [Hauchecorne and Chanin, 1980; Chanin and Hauchecorne, 1981; Chanin, 1986, 1987; Shibata et al., 1986].

In this report we present the results of 16 nights of Rayleigh scatter lidar measurements at Poker Flat, Alaska [65° 08' N, 147° 21' W], and Urbana, Illinois [40° 10' N, 88° 10' W], during which 42 monochromatic gravity wave events were identified and characterized. Both of the lidars used in this study for Rayleigh scatter measurements are relatively low-performance systems when compared to state-of-the-art Rayleigh lidars. However, their temporal and spatial resolutions are sufficient to observe monochromatic gravity wave events and to measure the critical wave parameters. In Section 2 the theoretical expressions used to estimate the atmospheric density response to a monochromatic gravity wave event are derived. The data processing technique used to estimate the vertical wavenumber spectrum of horizontal velocity from the measured density perturbations is discussed in Section 3. Representative examples of observed wave events are illustrated in Section 4. Seasonal variations in the measured gravity wave parameters and the relationships between them are presented and compared to previous radar and lidar observations in Sections 5 and 6. Altitude variations of rms wind perturbations are examined in Section 7. Rayleigh lidar performance and data processing tradeoffs are discussed in Appendix A.

2. ATMOSPHERIC DENSITY RESPONSE

The atmospheric density response to wave motions is governed by the continuity equation. By neglecting diffusion, Gardner and Shelton [1985] have shown that the density response can be written in the form

$$\rho(z,t) = e^{-\phi}\,\rho_o(z - \theta_z) \tag{1}$$

where

$\rho(z,t)$ = atmospheric density;

$\rho_o(z)$ = steady-state atmospheric density in the absence of wind perturbations;

$$\phi(\underline{r}, t) \approx \int_{-\infty}^{t} \nabla \cdot \underline{v}\, d\tau \tag{2}$$

$$\theta_z(\underline{r}, t) \approx \int_{-\infty}^{t} v_z\, d\tau \tag{3}$$

$\underline{r} = x\,\hat{x} + z\,\hat{z}$ = position vector where x is horizontal coordinate and z is vertical coordinate.

The wind vector is defined as

$$\underline{v} = v_x\hat{x} + v_z\hat{z}\ . \tag{4}$$

For gravity wave perturbations, the polarization and dispersion relations can be used to show that

$$\theta_z = \gamma H \phi \tag{5}$$

where γ is the ratio of specific heats and H is the atmospheric scale height. In an isothermal atmosphere the steady-state density decreases exponentially with altitude so that for gravity wave perturbations Eq. (1) becomes

$$\rho(z, t) = e^{(\gamma - 1)\phi}\,\rho_o(z)\ . \tag{6}$$

For our purposes it is most convenient to work with the natural logarithm of the relative density perturbations

$$r(z, t) = \ln(\rho/\rho_o) = (\gamma - 1)\,\phi = \left(\frac{\gamma - 1}{\gamma H}\right)\theta_z\ . \tag{7}$$

The gravity wave polarization and dispersion relations can be used to relate the vertical wavenumber spectra and mean-square values of ϕ and θ_z to the power spectrum $E_x(k_z)$ and mean-square value of the horizontal winds $< v_x^2 >$,

$$E_x(k_z) = (\gamma H N)^2 E_\phi(k_z) = N^2 E_{\theta_z}(k_z) \tag{8}$$

$$\langle v_x^2 \rangle = (\gamma H N)^2 \langle \phi^2 \rangle = N^2 \langle \theta_z^2 \rangle \ , \tag{9}$$

where $N = [(\gamma - 1)g/\gamma H]^{1/2}$ is the Brunt-Vaisala frequency. As a consequence of Eqs. (7) - (9), the gravity wave spectrum and mean-square wind velocity can be expressed in terms of the Fourier transform and mean-square value of r(z,t)

$$E_x(k_z) = \left(\frac{\gamma H N}{\gamma - 1}\right)^2 \frac{\langle |R(k_z)|^2 \rangle}{2L} \tag{10}$$

$$\langle v_x^2 \rangle = \left(\frac{\gamma H N}{\gamma - 1}\right)^2 \langle r^2(z, t) \rangle \tag{11}$$

where

$$R(k_z) = \int_{z_o - L/2}^{z_o + L/2} r(z, t)\, e^{i k_z z}\, dz \tag{12}$$

and L is the altitude range of observations and z_o is the altitude at the center of the observation interval.

For the case of low-frequency monochromatic waves, exact solutions for ϕ and θ_z were derived by Gardner and Shelton [1985]

$$\phi = \ln\left[1 + \frac{Ae^{\beta z}}{\gamma - 1} \cos(\omega t - \underline{k} \cdot \underline{r})\right] \tag{13}$$

$$\theta_z = \gamma H \ln\left[1 + \frac{Ae^{\beta z}}{\gamma - 1} \cos(\omega t - \underline{k} \cdot \underline{r})\right] \tag{14}$$

where

$Ae^{\beta z}$ = wave amplitude;

β = amplitude growth factor;

ω = wave frequency;

$\underline{k} = k_x \hat{x} + k_z \hat{z}$ = wavenumber vector;

k_x = horizontal wavenumber;

k_z = vertical wavenumber.

The corresponding vertical and horizontal winds generated by the gravity wave are given by [Hines, 1960]

$$v_z \approx - \frac{\gamma H N}{\gamma - 1} \frac{\lambda_z}{\lambda_x} A e^{\beta z} \sin(\omega t - \underline{k} \cdot \underline{r}) \tag{15}$$

$$v_x \approx \frac{\gamma H N}{\gamma - 1} A e^{\beta z} \sin(\omega t - \underline{k} \cdot \underline{r}) \ . \tag{16}$$

The vertical and horizontal wavelengths are respectively, λ_z and λ_x. The linear density perturbation is obtained by substituting Eq. (13) into (7) and noting that the wave amplitude is small (< 10%)

$$r(z, t) = (\gamma - 1) \ln \left[1 + \frac{A e^{\beta z}}{\gamma - 1} \cos(\omega t - \underline{k} \cdot \underline{r}) \right] \approx A e^{\beta z} \cos(\omega t - \underline{k} \cdot \underline{r}) \ . \tag{17}$$

Because the density perturbation, r(z,t), and horizontal velocity perturbation, v_x, are proportional and 90° out of phase, their respective power spectra are proportional, and Eqs. (10) and (11) result.

The kinetic energy of a monochromatic wave is defined as

$$KE(\underline{k}, \omega) = \frac{1}{2} |v_x|^2 + \frac{1}{2} |v_z|^2 \tag{18}$$

where v_x and v_z are the complex amplitudes of the horizontal and vertical wind velocities. For low-frequency waves $\lambda_z << \lambda_x$, so that

$$KE(\underline{k}, \omega) \approx \frac{1}{2} |v_x|^2 = \frac{1}{2} \left(\frac{\gamma H N}{\gamma - 1} \right)^2 (A e^{\beta z})^2 \ . \tag{19}$$

The presence of monochromatic waves in the lidar profiles of r(z, t) can be determined by examining the gravity wave spectrum. The spectral signature for a monochromatic wave is computed using Eqs. (10), (12), and (17)

$$E_x(k_z) = \frac{1}{2L} \left(\frac{\gamma H N}{\gamma - 1} \right)^2 (A e^{\beta z_o})^2 \left[\frac{\cosh(\beta L) - 1}{2 [(k - k_z)^2 + \beta^2]} + \frac{\sin^2 [L(k - k_z)/2]}{[(k - k_z)^2 + \beta^2]} \right] . \tag{20}$$

Equation (20) is plotted in Figure 1 for λ_z = 7.5 km, $A e^{\beta z} = 0.01$, L = 15 km and several values of β. The spectral peak occurs at the spatial frequency λ_z^{-1}, and the magnitude in m^3/s^2 is

$$E_x(2\pi/\lambda_z) = \frac{L}{8} \left(\frac{\gamma H N}{\gamma - 1} \right)^2 (A e^{\beta z_o})^2 \left[\frac{\sinh(\beta L/2)}{(\beta L/2)} \right]^2 = \frac{L}{4} KE(z_o) \left[\frac{\sinh(\beta L/2)}{(\beta L/2)} \right]^2 . \tag{21}$$

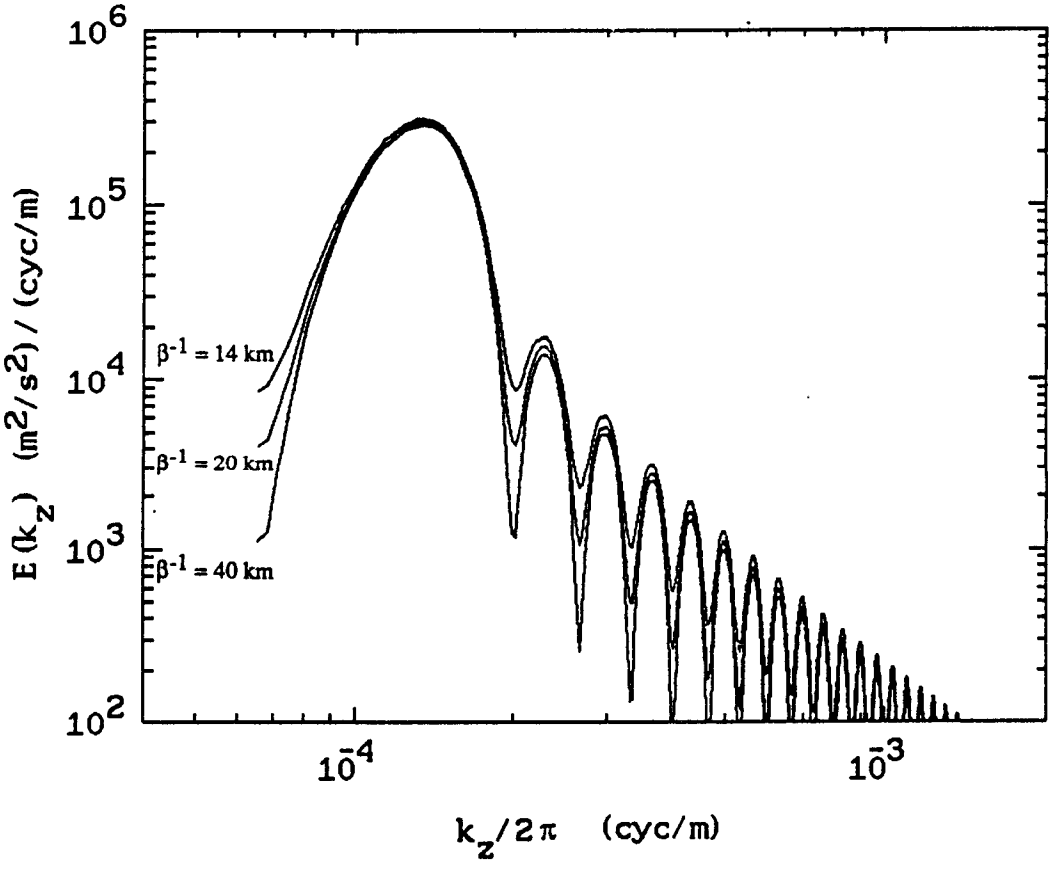

Figure 1. Simulated vertical wavenumber spectrum for Rayleigh scatter observations with $\lambda_z = 7.5$ km, $Ae^{\beta z} = 1$ %, L = 15 km and $\beta^{-1} = 14$ km, 20 km and 40 km.

For most of the data reported here, $\beta L \leq 1$, so that the square of the bracketed term in Eq. (21) is approximately 1. The vertical wavelength of a monochromatic wave can be determined by measuring the spatial frequency of the spectral peak. The wave amplitude and kinetic energy at altitude z_o can be computed from the magnitude of the spectral peak using Eq (21). The vertical phase velocity (c_z) of the wave is measured directly from the density perturbation profiles.

3. EXPERIMENTAL DATA

Data used in this study were obtained at Poker Flat, Alaska, during February and March 1986, with the Air Force Geophysics Laboratory (AFGL) mobile Rayleigh lidar and at Urbana, Illinois, by using the Rayleigh scatter photocounts from lidar profiles measured during 1984-86 with the UIUC sodium lidar system. The AFGL Rayleigh lidar uses an Nd:YAG laser operating at a wavelength of 532 nm and is described by Philbrick et al. [1987]. The UIUC lidar utilizes a flashlamp-pumped dye laser tuned to the sodium resonance line at 589 nm. The operational characteristics of the UIUC lidar system are described in Gardner et al. [1986]. The parameters of the AFGL and UIUC lidars are compared in Table 1.

While both the AFGL and UIUC lidar systems count backscattered photons from a single laser shot in discrete time intervals that correspond to range bins, the form of the Alaska and Urbana data sets used in this study are slightly different. AFGL Rayleigh lidar data consist of atmospheric density profiles with a range resolution of 300 m. The density profiles were generated from 5-minute photocount profiles obtained by accumulating the returns from 3000 laser shots. Absolute density was computed by referencing photocounts near 25 km altitude to an independent measurement of atmospheric density. Urbana lidar data consist of 1-minute photocount profiles with a range resolution of 150 m obtained by integrating backscattered photocounts from 250 laser shots.

Photocount profiles can be contaminated by Mie scattering due to atmospheric aerosols. Both Rayleigh and Mie scattering are caused by the presence of particles in the propagation path of a laser beam. However, Rayleigh scattering is applicable for gaseous atmospheric molecules comprising the air when the radius of the scattering particle satisfies the condition $r \leq 0.03\lambda$, while Mie scattering applies to aerosols and particulates such as volcanic ash, meteoric dust and water droplets in clouds [Cerny and Sechrist, 1980]. Methods to detect the presence of aerosols and determine regions of pure Rayleigh scattering use two lasers operating at distinct frequencies to exploit the different wavelength dependence of Mie (λ^{-1}) and Rayleigh (λ^{-4}) scattering cross sections. These analyses typically show no aerosols above 25-30 km [Chanin and Hauchecorne, 1981; Philbrick et al., 1987]. In the UIUC lidar profiles the Rayleigh scatter altitudes are also limited by electronic PMT blanking designed to prevent receiver overload from high backscatter returns at lower altitudes. The PMT gain is switched to maximum at an altitude near 32-35 km in most profiles obtained with the UIUC lidar. The maximum altitude range of observations for Rayleigh lidar measurements is constrained by system noise.

Rayleigh scatter photocount data can be readily converted to density perturbation measurements, since range-scaled signal photocounts are proportional to atmospheric density, provided there is no aerosol scattering. Atmospheric density is estimated from measured photocount data by range scaling and multiplying signal photocounts by a scaling constant ξ,

TABLE 1. Comparison of Lidar System Parameters

Parameter	AFGL Rayleigh Lidar	UIUC Sodium Lidar
Laser Type	Nd:YAG	Flashlamp Pumped Dye
Wavelength, λ	532 nm	589 nm
Energy/Pulse, E_L	300 mJ	20 mJ
Pulse Rate, R	10 Hz	5 Hz
Bin Resolution, Δz	300 m	150 m
Receiver Area, A_r	0.07 m^2	1.2 m^2
Receiver Efficiency, η	0.05	0.05

$$\rho(z,t) = \xi z^2 \left[N(z,t) - N_B(t) \right] \tag{22}$$

where N(z,t) is the photocount at altitude z measured at observation time t and $N_B(t)$ is the background photocount per range bin. The scaling constant ξ is related to the total photocounts measured over the altitude range of observations at time t. Density perturbation at altitude z and time t is defined by

$$r(z,t) = \frac{\rho(z,t) - \rho_o(z)}{\rho_o(z)} = \frac{\rho(z,t)}{\rho_o(z)} - 1 \; . \tag{23}$$

Measured photocounts are used to estimate $\rho(z,t)$ and $\rho_o(z)$ and calculate the density perturbation,

$$r(z,t) = \frac{\xi z^2 \left[N(z,t) - N_B(t) \right]}{\zeta z^2 \left[N(z) - N_B \right]} - 1 \tag{24}$$

where N(z) is the average measured photocounts at altitude z and N_B is the average background photocounts per range bin. The scaling constant ζ is a function of the total photocounts in the average profile for the evening's observations.

The estimated vertical wavenumber spectrum obtained from Rayleigh scatter photocount data contains a signal component $E_x(k_z)$ contaminated by shot noise. While the resolution of lidar profiles is fundamentally governed by the width of the receiver range-gate and sampling time interval, the practical resolution limits are determined by shot noise, which is a function of laser power, receiver telescope area, integration time and observation range. The expected vertical wavenumber spectrum obtained by scaling the spatial power spectrum of the density perturbations as in Eq. (10) will have the form

$$\frac{1}{2L}\left(\frac{\gamma H N}{\gamma - 1}\right)^2 < \left| R(k_z) \right|^2 > \approx E_x(k_z) + \frac{1}{2L}\left(\frac{\gamma H N}{\gamma - 1}\right)^2 \frac{H^2}{N_T}\left(1 + \frac{L - H}{z_o}\right)^2 e^{L/H} \; . \tag{25}$$

The first term on the right side of Eq. (25) is the desired vertical wavenumber spectrum while the second term is the shot noise component. The linear saturation theory predicts that the vertical wavenumber spectra of horizontal wind perturbations have a k_z^{-3} dependence and magnitude given by [Dewan and Good, 1986; Smith et al., 1987]

$$E_x(k_z) = \frac{N^2}{2 k_z^3} \; . \tag{26}$$

Equation (26) must be greater than the shot noise floor in order to reliably measure wave parameters. Shorter wavelengths can only be observed by decreasing the shot noise contamination. The shot noise floor is reduced by increasing N_T, the total signal photocount in a

profile, or by reducing the altitude range of observations, L. However, longer integration periods needed to increase N_T reduce the temporal resolution and may average out wave events with shorter periods. Decreasing the altitude range of observation will also exclude measurements of longer wavelength events. Equation (25) is derived in Appendix A and is used to predict the spatial resolution of Rayleigh lidar measurements based on the model spectrum.

The procedure used to process photocount data from Rayleigh scatter altitudes is similar to the method that has been effectively used to process UIUC sodium lidar data since 1978 [Rowlett et al., 1978]. Photocount data are integrated over adjacent observation times to reduce shot noise levels. Density perturbation profiles are then calculated from the integrated photocount profiles. The vertical wavenumber spectrum of each profile is obtained by scaling the spatial power spectrum of the density perturbation profile as in Eq. (10). Vertical wavelength (λ_z) and energy density $E_x(k_z)$ are measured from the vertical wavenumber spectrum. Each density perturbation profile is spatially lowpass filtered in the Fourier domain to reduce high frequency shot noise. Vertical phase velocity (c_z) is then estimated by observing the phase progression of the waves in the spatially filtered perturbation profiles. Other characteristics of discrete wave events are inferred from the measured parameters.

4. GRAVITY WAVE CASE STUDIES

To illustrate the analysis technique we now discuss several wave events observed during 3 nights of measurements at Poker Flat, Alaska, using the AFGL Rayleigh lidar, and 13 nights at Urbana, Illinois, with the UIUC lidar system. These sixteen observation nights include nearly 100 profiles. Alaska data were examined in an altitude region from 25 km up to 55 km and integrated for measurement periods of 20 and 30 minutes. Urbana photocount profiles were integrated for 60-minutes and limited to a maximum observation range of 15 km. The altitude range for the Urbana data was usually 35-50 km.

The data measured on February 24, 1986 at Poker Flat with the AFGL Rayleigh lidar were integrated to obtain 20-minute density perturbation profiles. Due to the intermittent spacing between measured profiles the data collected represent only a fraction of the night. The altitude range of observation was 25-55 km with a 300 m vertical resolution. The spatial power spectrum of each density perturbation profile was computed by calculating the magnitude squared of the discrete Fourier transformed data. A raised cosine tapering function was used to window the spatial profile in order to control sidelobe effects in the power spectrum. The vertical wavenumber spectrum of horizontal velocity was then obtained by scaling this spatial power spectrum by $[\gamma HN/(\gamma - 1)]^2/2L$ as described by Eq. (10). The spatial power spectra obtained during the evening's observations were averaged to reduce the variance of the spectral estimate. The average vertical wavenumber spectrum for February 24, 1986 is shown in Figure 2. Energy density $E_x(k_z)$ is plotted versus vertical wavenumber $k_z/2\pi$, from L^{-1} to the Nyquist frequency $(2\Delta z)^{-1}$, where L = 30 km is the observation range and Δz = 300 m. The dashed line is the estimated shot noise floor. A spectral peak near $k_z/2\pi = 1.3 \times 10^{-4}$ cyc/m (λ_z = 7.7 km) dominates the power spectrum. The signal-to-noise ratio at this peak is almost 10 dB. The amplitude of the gravity wave event calculated using Eq. (21) is 4% at z_o = 40 km. This corresponds to a wind amplitude of 20 m/s and a kinetic energy density of 192 m^2/s^2.

The spatial lowpass filter cutoff is the vertical wavenumber where the average spectral energy approaches the shot noise floor. The Poker Flat data measured on February 24 was spatially filtered with a cutoff wavenumber of 2×10^{-4} cyc/m. Wave-like structures are clearly present in the spatially filtered density perturbation profiles. In particular, the four consecutive profiles corresponding to the observation interval 07:14 to 10:26 (UTC) shown in Figure 3 clearly exhibit a wave structure with downward phase progression. A vertical phase velocity of 0.3 m/s is calculated from the slope of the phase progression. The observed period of the 7.7 km wave is 430 minutes.

Atmospheric gravity waves do not necessarily exhibit pure monochromatic behavior, and the presence of waves with shorter vertical wavelengths can obscure longer wavelength waves. The vertical wavenumber spectrum shown in Figure 4 was obtained by averaging the spectra of

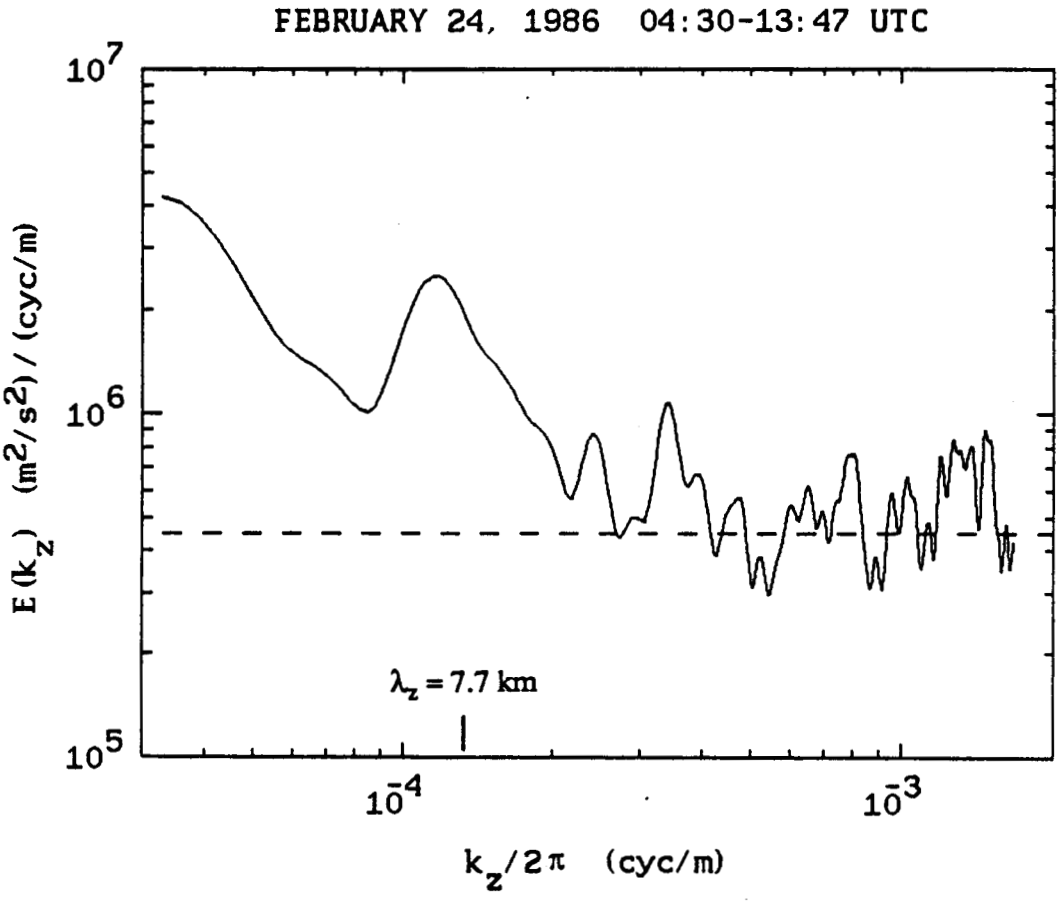

Figure 2. Average vertical wavenumber spectrum measured during 04:30 to 13:47 (UTC) on February 24, 1986 using the AFGL Rayleigh lidar at Poker Flat, AK. The altitude range of observations is 25-55 km and the vertical resolution is 300 m. The dashed line is the estimated shot noise level.

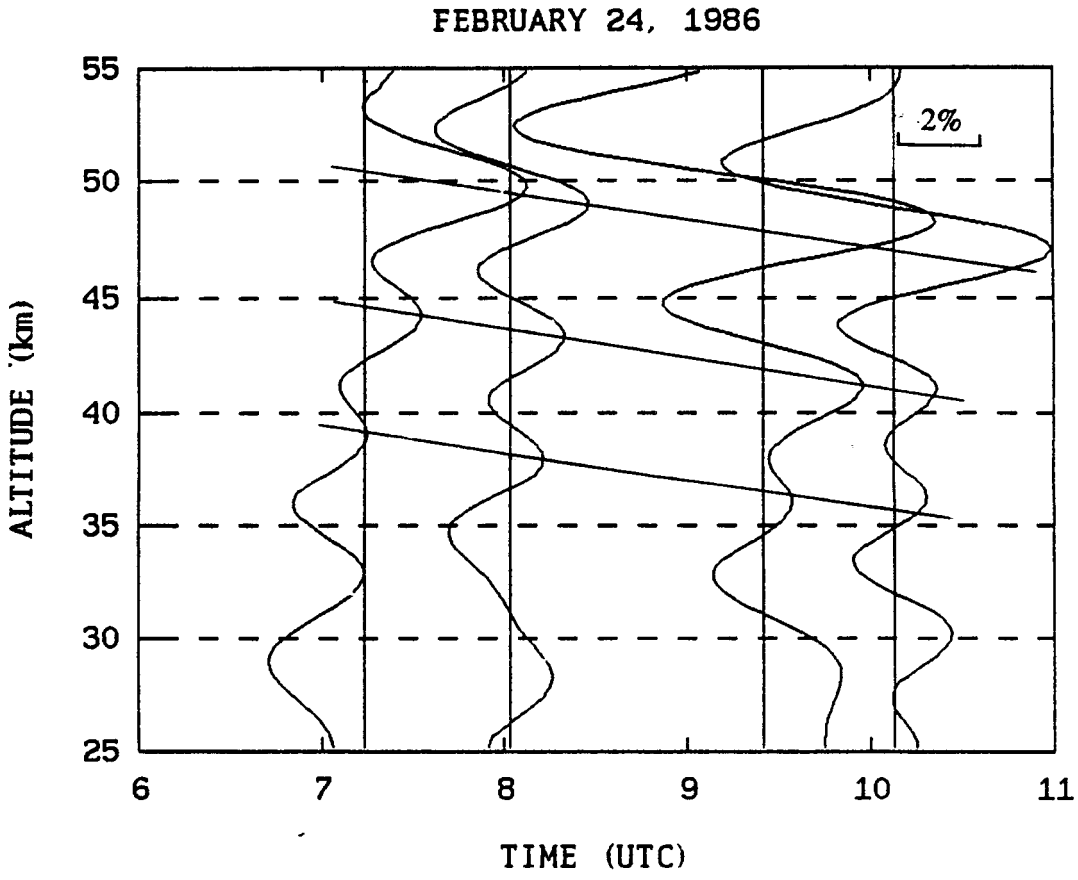

Figure 3. Spatially filtered density perturbation profiles measured on February 24, 1986 using the AFGL Rayleigh lidar at Poker Flat, AK. The low-pass filter cutoff wavenumber was 2 x 10^{-4} cyc/m corresponding to a cutoff wavelength of 5 km. The diagonal lines indicate the 0.3 m/s phase progression of the 7.7 km wave.

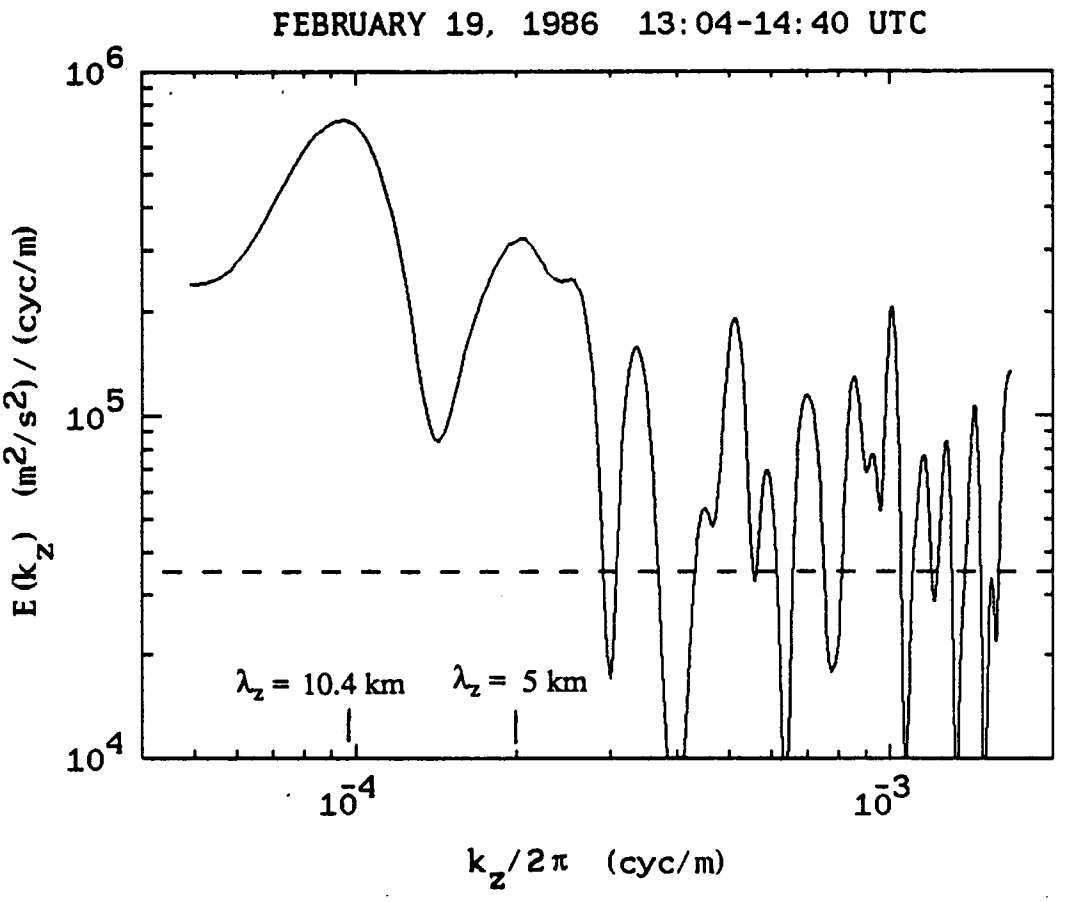

Figure 4. Average vertical wavenumber spectrum measured during 13:04 to 14:40 (UTC) on February 19, 1986 using the AFGL Rayleigh lidar at Poker Flat, AK. The altitude range of observations is 25-45 km and the vertical resolution is 300 m. The dashed line is the estimated shot noise level.

two 30-minute profiles measured on February 19, 1986 at Poker Flat using the AFGL lidar. The altitude range of observation was 25 to 45 km. As expected with a longer integration time and decreased altitude range of observation, the noise floor for February 19 is a decade lower than the noise floor for February 24. Two peaks at vertical wavenumbers of 9.6×10^{-5} and 2×10^{-4} cyc/m, corresponding respectively to wavelengths of 10.4 km and 5 km, are clearly evident in the power spectrum. The signal-to-noise ratio for the main lobe in the spectrum is 14 dB. The two profiles, spatially filtered at a cutoff wavenumber of 3×10^{-4} ($\lambda_z = 3.3$ km), are plotted in Figure 5. The slope of the downward phase progression of the wave-like structures indicates a phase velocity of 0.5 m/s. By selecting a cutoff wavenumber of 1.33×10^{-4} cyc/m that passes only energy of the longer wavelength event, we can measure the 0.65 m/s downward phase progression of the 10.4 km wave shown in Figure 6.

Short wavelength events were observed in the March 8, 1986 Poker Flat data by reducing the altitude range of observations to 15 km. Figure 7 illustrates the temporal variations of the 20-minute profiles that were spatially low-pass filtered with a cutoff wavelength of 2.5 km. Events with 3 km wavelengths are observed in Figure 7, with measured phase velocities of 1 m/s and 0.83 m/s. The observed periods for these two wave events are on the order of 50 minutes.

Lidar data taken at Urbana with the UIUC lidar system were processed in a similar fashion. However, differences in operating characteristics of the AFGL and UIUC lidar systems necessitated longer integration times and reduced observation range for the UIUC data. Photocount data collected on August 13-14, 1984 were integrated over 60-minute measurement periods, during which the laser was fired approximately 20,000 times. Six profiles were obtained by extracting Rayleigh scatter photocount data from the sodium lidar profiles over the 35-50 km altitude range. A perturbation about the mean density was computed at every range bin for each 60-minute profile. The average vertical wavenumber spectrum for observations on this night is illustrated in Figure 8. A spectral peak is clearly evident at $k_z/2\pi = 1.3 \times 10^{-4}$ cyc/m ($\lambda_z = 7.7$ km). The signal-to-noise ratio at this peak is 7 dB. The spatially filtered profiles shown in Figure 9 indicate an apparent 0.32 m/s downward phase progression of the 7.7 km gravity wave.

Smaller vertical wavelengths were also observed in the Urbana data. Figure 10 shows the spatially low-pass filtered Rayleigh lidar profiles for Urbana data measured on February 29 - March 1, 1984. The spatial cutoff wavelength is 1.8 km. A vertical wavelength near 2.4 km and 0.25 m/s downward phase progression is evident in the data.

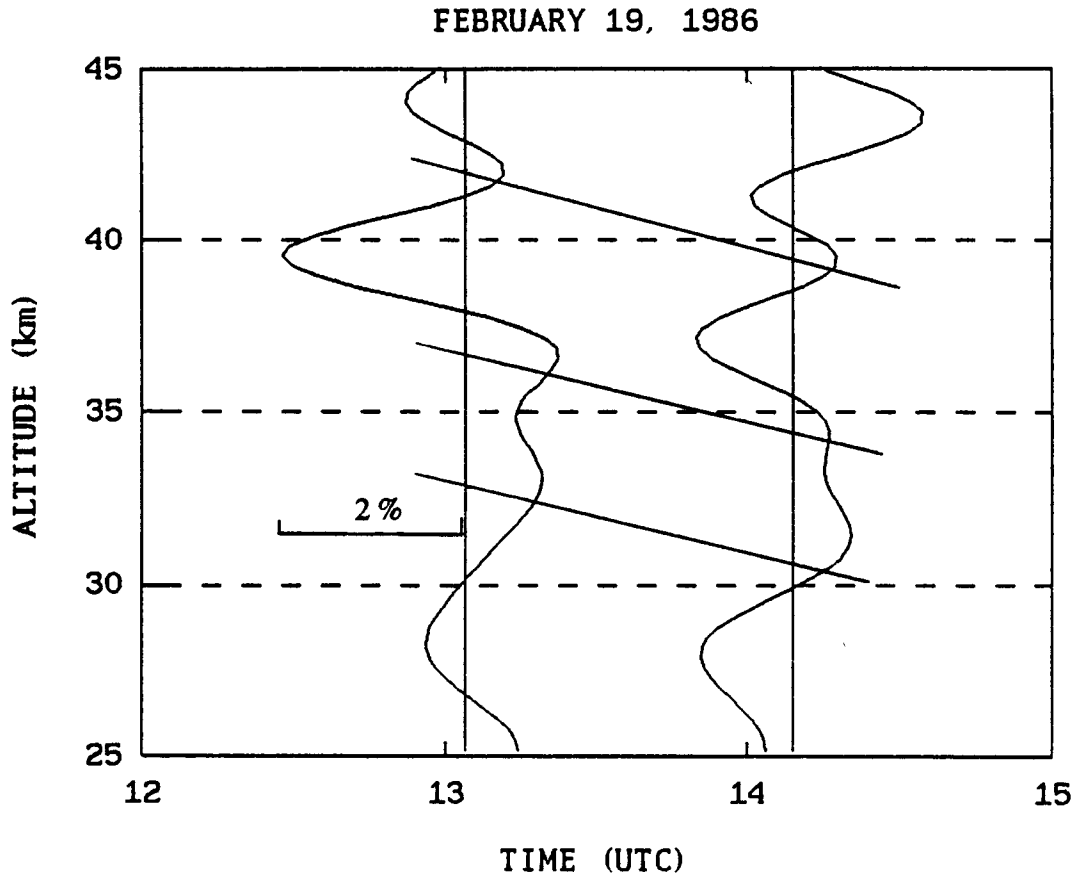

Figure 5. Spatially filtered density perturbation profiles measured on February 19, 1986 using the AFGL Rayleigh lidar at Poker Flat, AK. The low-pass filter cutoff wavenumber was 2.67 x 10^{-4} cyc/m corresponding to a cutoff wavelength of 3.75 km. The diagonal lines indicate the 0.5 m/s phase progression of the 5 km wave.

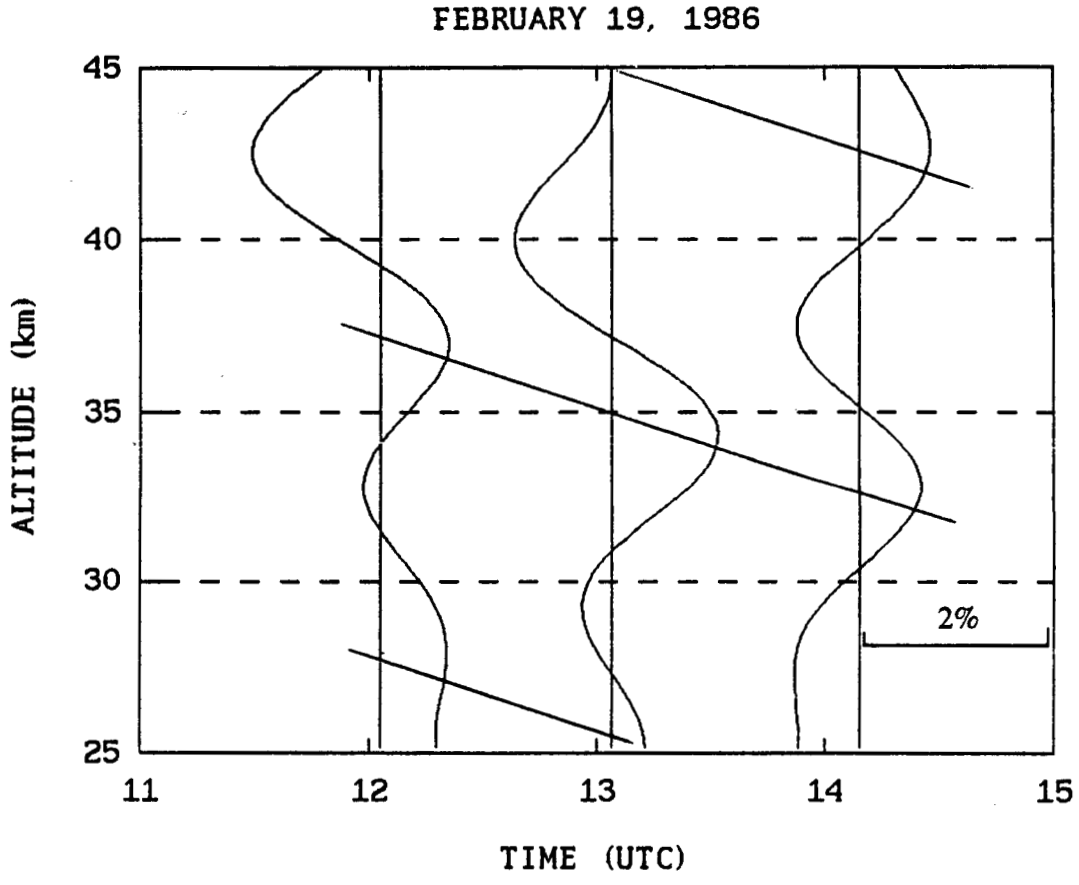

Figure 6. Spatially filtered density perturbation profiles measured on February 19, 1986 using the AFGL Rayleigh lidar at Poker Flat, AK. The low-pass filter cutoff wavenumber was 1.33×10^{-4} cyc/m corresponding to a cutoff wavelength of 7.5 km. The diagonal lines indicate the 0.65 m/s phase progression of the 10 km wave.

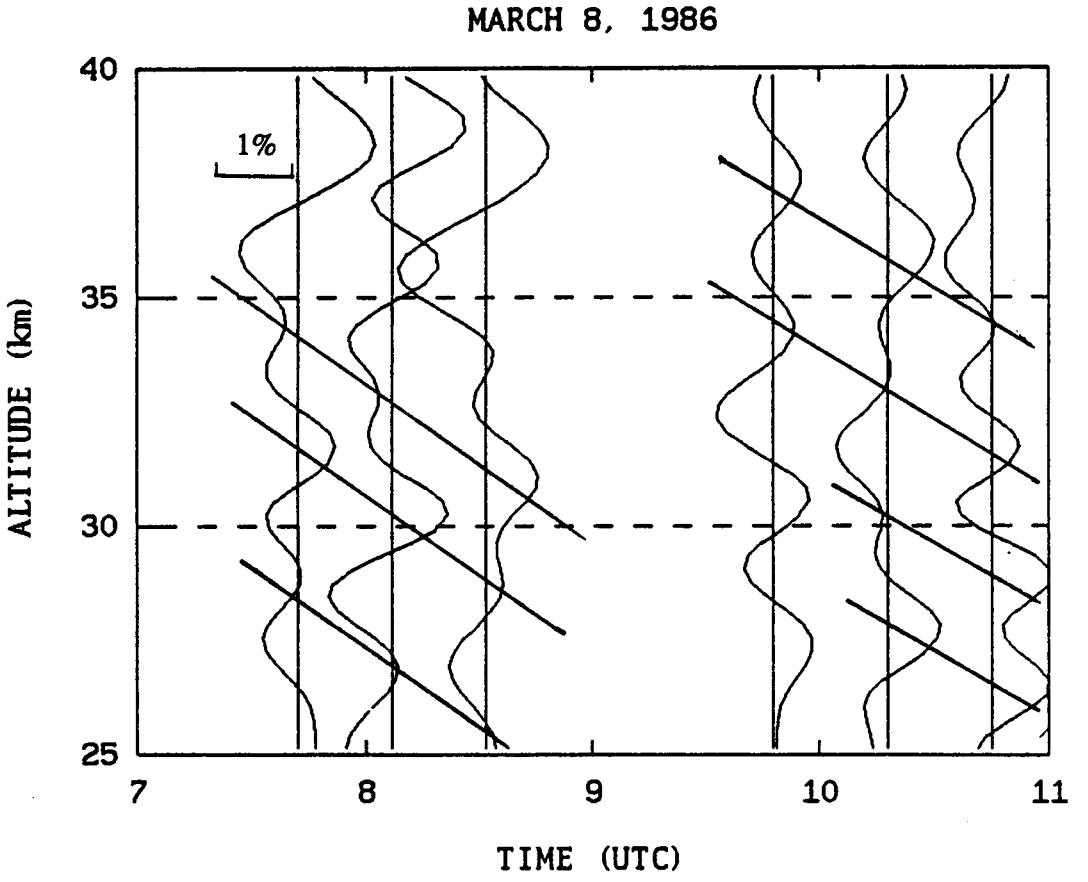

Figure 7. Spatially filtered density perturbation profiles measured on March 8, 1986 using the AFGL Rayleigh lidar at Poker Flat, AK. The low-pass filter cutoff wavenumber was 4 x 10^{-4} cyc/m corresponding to a cutoff wavelength of 2.5 km. The diagonal lines indicate the 1.0 m/s and 0.83 m/s phase progressions of the 3 km waves.

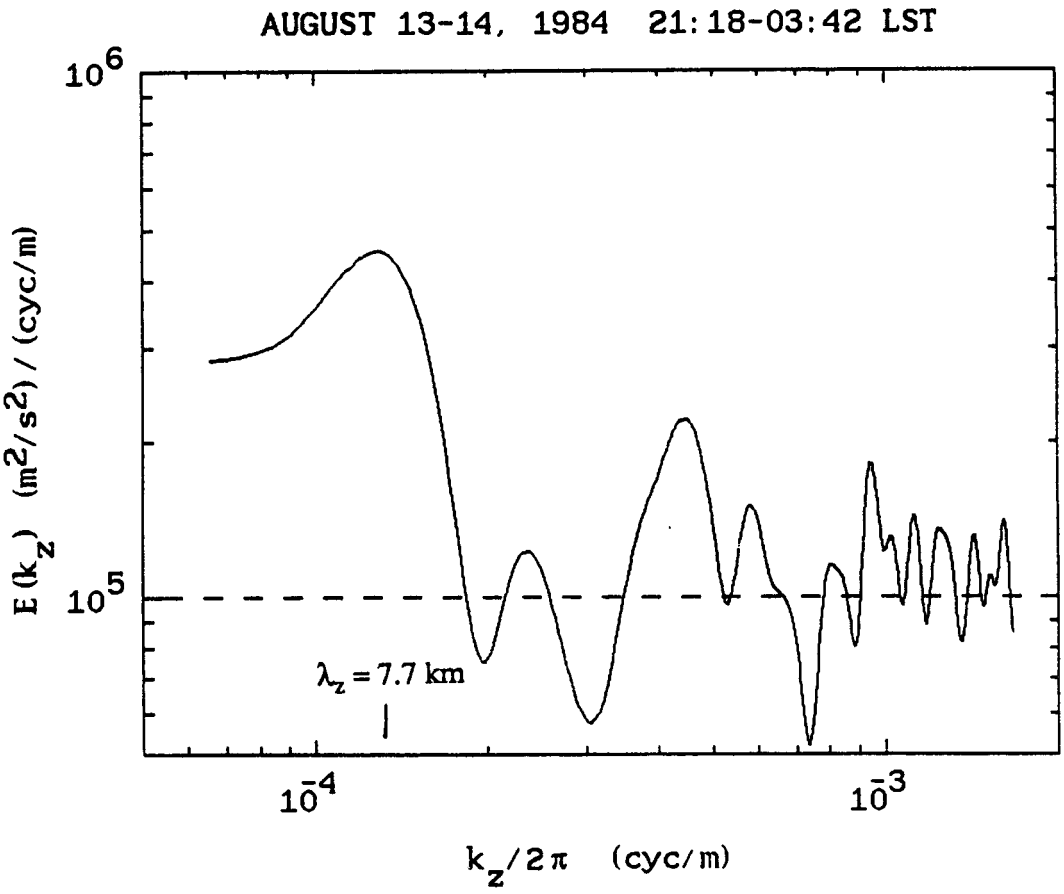

Figure 8. Average vertical wavenumber spectrum measured during 21:18 to 03:42 LST on August 13, 1984 using the UIUC lidar at Urbana, IL. The altitude range of observations is 35-50 km and the vertical resolution is 300 km. The dashed line is the estimated shot noise level.

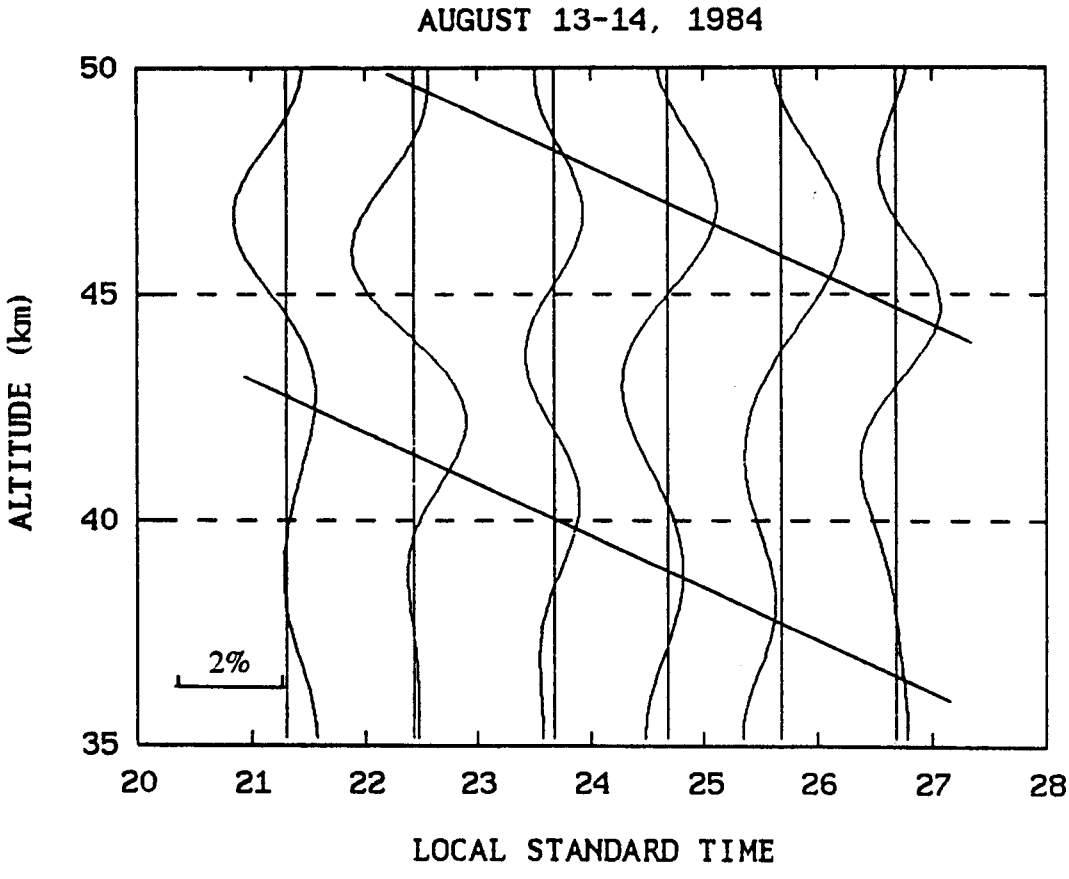

Figure 9. Spatially filtered density perturbation profiles measured on August 13, 1984 using the UIUC lidar at Urbana, IL. The low-pass filter cutoff wavenumber was 2×10^{-4} corresponding to a cutoff wavelength of 5 km. The diagonal lines indicate the apparent 0.32 m/s downward phase progression of the 7.7 km wave.

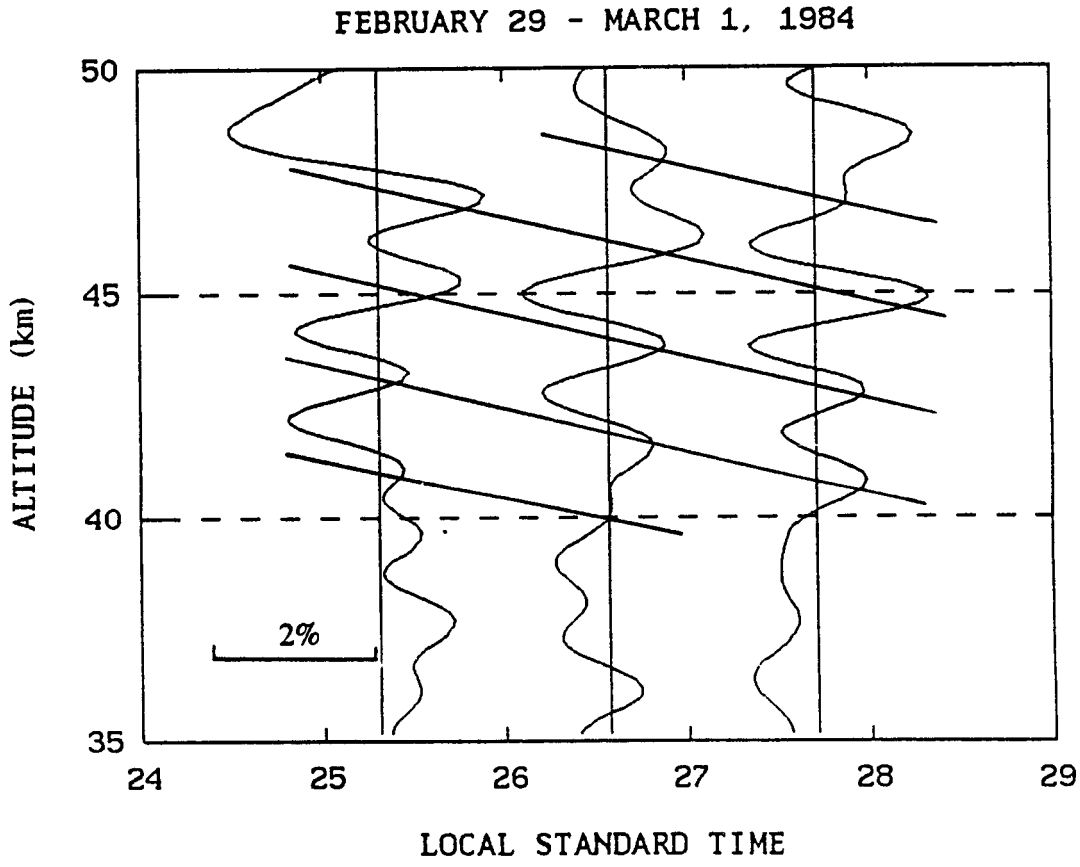

Figure 10. Spatially filtered density perturbation profiles measured on February 29 - March 1, 1984 using the UIUC lidar at Urbana, IL. The low-pass filter cutoff wavenumber was 5.5 x 10^{-4} corresponding to a cutoff wavelength of 1.8 km. The diagonal lines indicate the apparent 0.25 m/s downward phase progression of the 2.4 km wave.

5. SEASONAL VARIATION OF GRAVITY WAVE PARAMETERS

Wave-like structures were observed in almost all density perturbation profiles examined for this study. Coherent downward phase progression was identified in two or more consecutive profiles at least once during each of the 16 observation nights. Previous Rayleigh lidar observations in the 30-70 km altitude range indicated that wave structures are almost always present in the density profiles for 5- to 60-minute integration periods [Chanin and Hauchecorne, 1981]. A total of 42 monochromatic wave events were observed during the 16 nights. Six events were observed in the Alaska data during three nights of measurements, while the remaining 36 events were found in the Urbana data.

Vertical wavelength (λ_z), vertical phase velocity (c_z), and wave amplitude ($Ae^{\beta z}$) are measured directly from the lidar data. For each wave event, the observed period (T_{ob}) and horizontal wavelength (λ_x) are inferred from λ_z and c_z. The measured vertical wavelength, phase velocity, amplitude and inferred period of each gravity wave event identified during the 16 observation nights are summarized in Appendix B. Gravity wave parameters extracted from the Alaska and Urbana data are combined in the subsequent presentation.

The measured vertical wavelengths ranged from 2 to 11.5 km. The maximum λ_z that can be measured is limited by the altitude range of observations, while the minimum value is a function of system noise. Vertical wavelength is plotted versus observation date in Figure 11. No distinct seasonal variations are evident in the data. Dominant wave activity appears to occur at vertical wavelengths near 2-4 km and 7-10 km. The average vertical wavenumber spectrum for 6 of the 13 Urbana observation dates is shown in Figure 12. The average spectrum for the Urbana data indicates dominant wavelengths of 2-4 km and 7-10 km. These data correspond to an observation range of 35-50 km. All Urbana data sets are not included in this average spectrum because of the differences in the altitude region of observation. The altitude of maximum wind amplitude associated with 2-4 km vertical wavelength events is predicted to be between 40-60 km [Midgley and Leimohn, 1966]. Because wave events are most likely to be observed at altitudes where the wave amplitude is maximum, our data appear to be consistent with Midgley and Leimohn's predictions. The average vertical wavenumber spectrum for the three Alaska observation nights is shown in Figure 13. The observation range was 25-45 km. Signal energy at a vertical wavelength of 8 km is also quite apparent in this power spectrum.

The values of λ_z observed in this study correspond well with previous radar and lidar measurements. Rayleigh scatter studies with an XeF lidar at 30-65 km altitude range over Fukuoka, Japan, with 20-minute profile integration times and 1.5 km bin resolution indicate a dominant vertical wavelength near 10 km [Shibata et al., 1986]. Rayleigh lidar observations in the same altitude region over Haute Provence Observatory in France show dominant vertical wavelengths on the order of 8-15 km [Chanin and Hauchecorne, 1981; Chanin, 1986,1987].

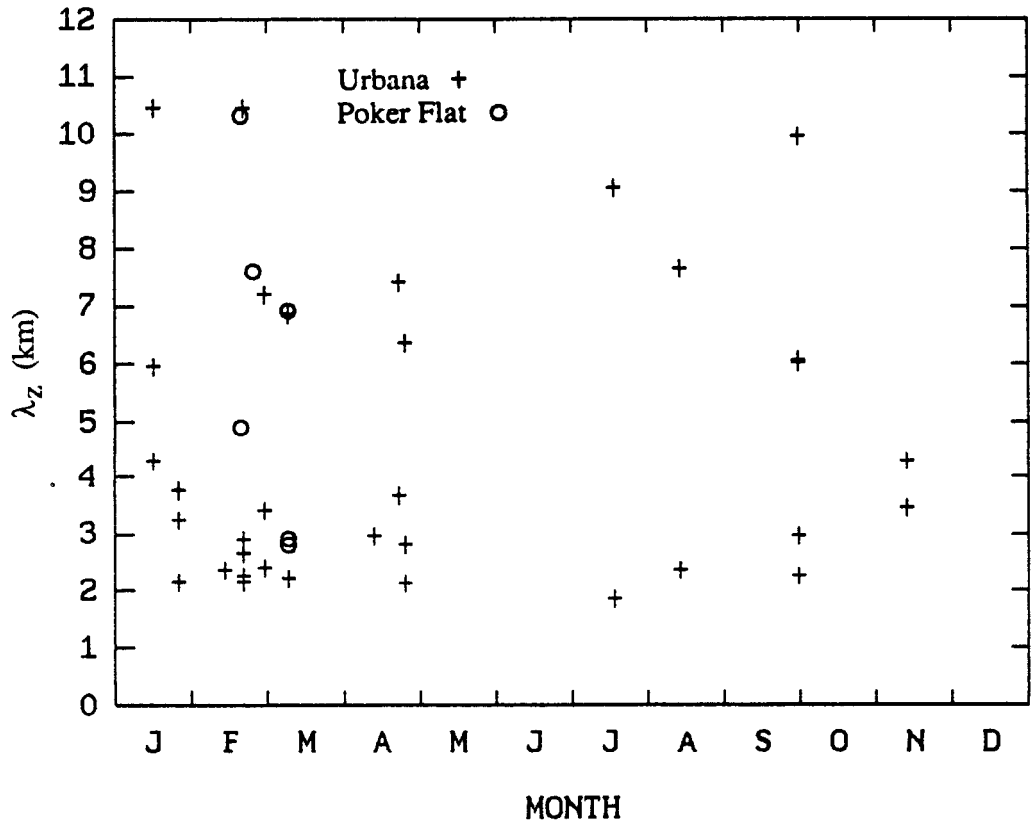

Figure 11. Seasonal distribution of vertical wavelengths.

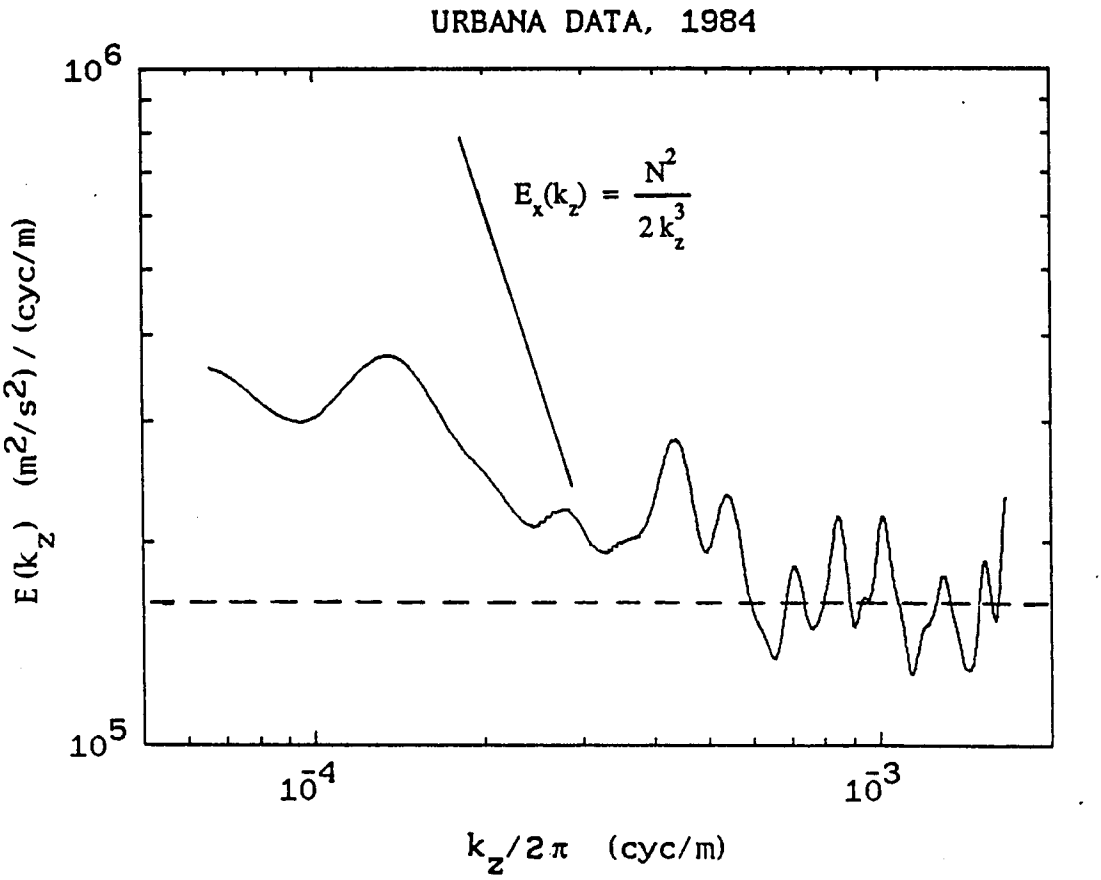

Figure 12. Average vertical wavenumber spectrum measured at Urbana, IL on February 20, March 8, July 17, August 13, September 30, and November 12, 1984 using the UIUC lidar. The altitude range of observations is 35-50 km with a spatial resolution of 300 m and a temporal resolution of 60 minutes. The dashed line is the estimated shot noise floor.

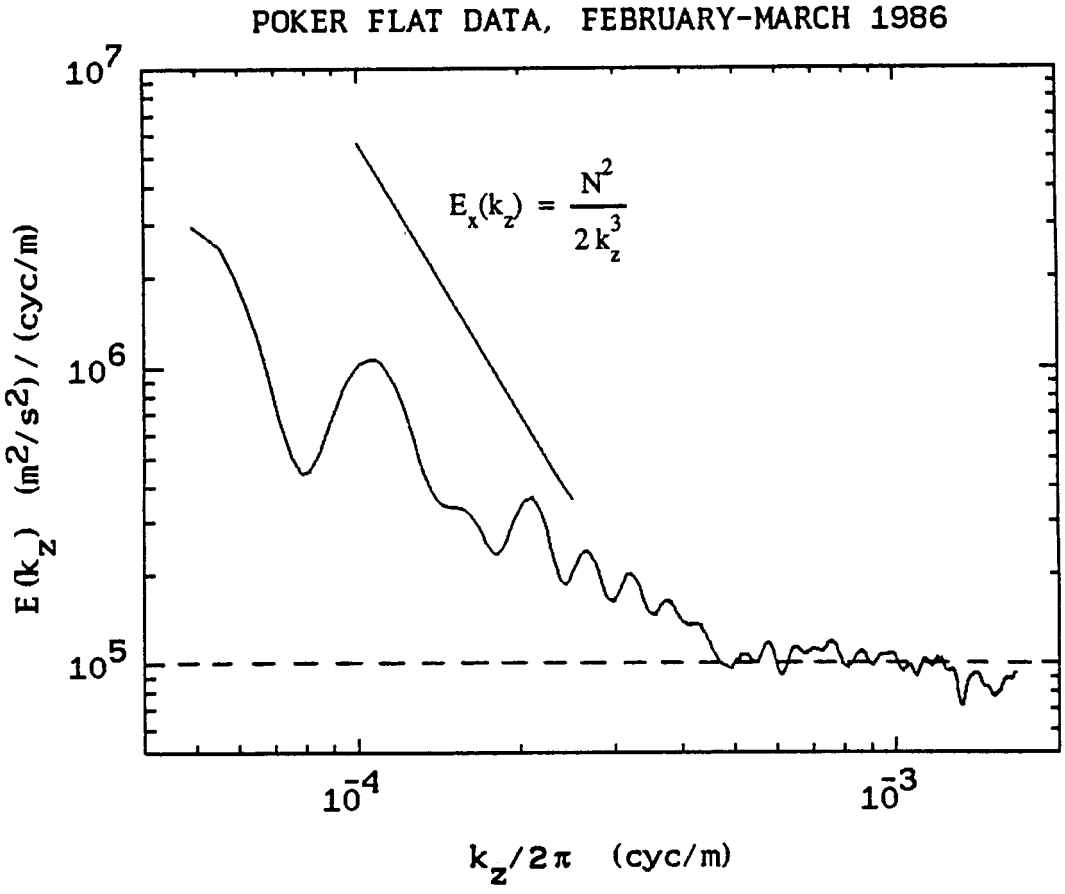

Figure 13. Average vertical wavenumber spectrum measured on February 19, February 24, and March 8, 1986 at Poker Flat, AK using the AFGL Rayleigh lidar. The altitude range of observations is 25-45 km with a spatial resolution of 300 m and a temporal resolution of 10 minutes.. The dashed line is the estimated shot noise floor.

Sodium lidar studies of the mesopause region (85-105 km) also show vertical wavelengths in the 2-15 km range [Gardner and Voelz, 1987]. Radar measurements of λ_z in the 60-110 km altitude region varied from 0.1-40 km with a median value of 10-15 km [Meek et al., 1985].

The vertical phase velocities of the upward propagating gravity waves ranged from 0.11 m/s to 1.0 m/s with a mean value of 0.39 m/s. Seasonal variations in vertical phase velocity are shown in Figure 14. Shibata et al. [1986] found vertical phase velocities ranging up to 0.33 m/s with minimums near zero in January and February. This particular trend is not seen in our data. Chanin and Hauchecorne [1981] reported that c_z is a function of altitude with measured values of c_z near 1 m/s at 50-70 km and less than 0.2 m/s below 50 km altitudes. Vertical phase velocities measured for gravity waves in the sodium layer (85-105 km) ranged from 0.2 to 1.75 m/s [Gardner and Voelz, 1987].

The observed period of each gravity wave event was inferred from measurements of the vertical wavelength and vertical phase velocity. Values of observed wave period ranged from 50 to 1000 minutes with a mean value of 240 minutes. The lower value is limited by the 20-, 30-, and 60-minute integration times associated with the individual profiles. Due to the presence of background wind fields, the observed frequency of the wave is the Doppler-shifted frequency rather than the intrinsic frequency. For lidar measurements the observed periods will be biased to values larger than the corresponding intrinsic wave periods [Gardner and Voelz, 1987]. The seasonal distribution of T_{ob} is shown in Figure 15. Sodium lidar studies did not observe wave events with periods greater than 200 minutes in summer observations [Gardner and Voelz, 1987]. The wave periods of the few summer events seen in the data presented here exceed 200 minutes. However, there does appear to be a slight trend towards shorter wave periods in summer. The radar technique used in Meek et al. [1985] enabled measurements of background winds in the direction of wave propagation that were used to compute Doppler shifts and estimate T, the intrinsic period of each wave. Observed wave periods varied between 5 and 500 minutes while intrinsic periods were as long as 900 minutes.

For low-frequency gravity waves, the horizontal wavelength associated with a given vertical wavelength and wave period is calculated by applying the dispersion relation. The inferred horizontal wavelengths ranged from 40 km to nearly 2000 km. Seasonal variations in horizontal wavelengths are shown in Figure 16. Sodium lidar studies did not observe wave events with horizontal wavelengths greater than 400 km in summer observations [Gardner and Voelz, 1987]. However, no seasonal trends are evident in the data presented here, and the horizontal wavelengths of the few summer events seen in this data set exceed 400 km. Meek et al. [1985] measured horizontal wavelengths between 45 and 300 km using MF radar and and an array of three receiving antennas.

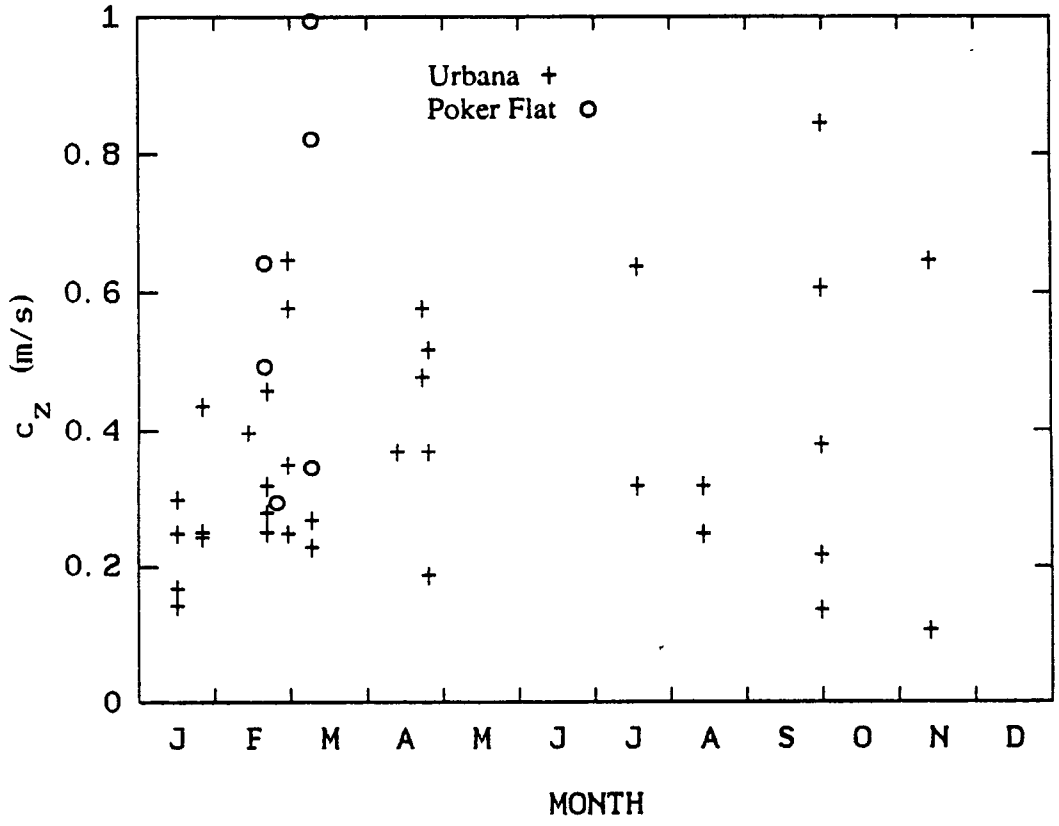

Figure 14. Seasonal distribution of vertical phase velocities.

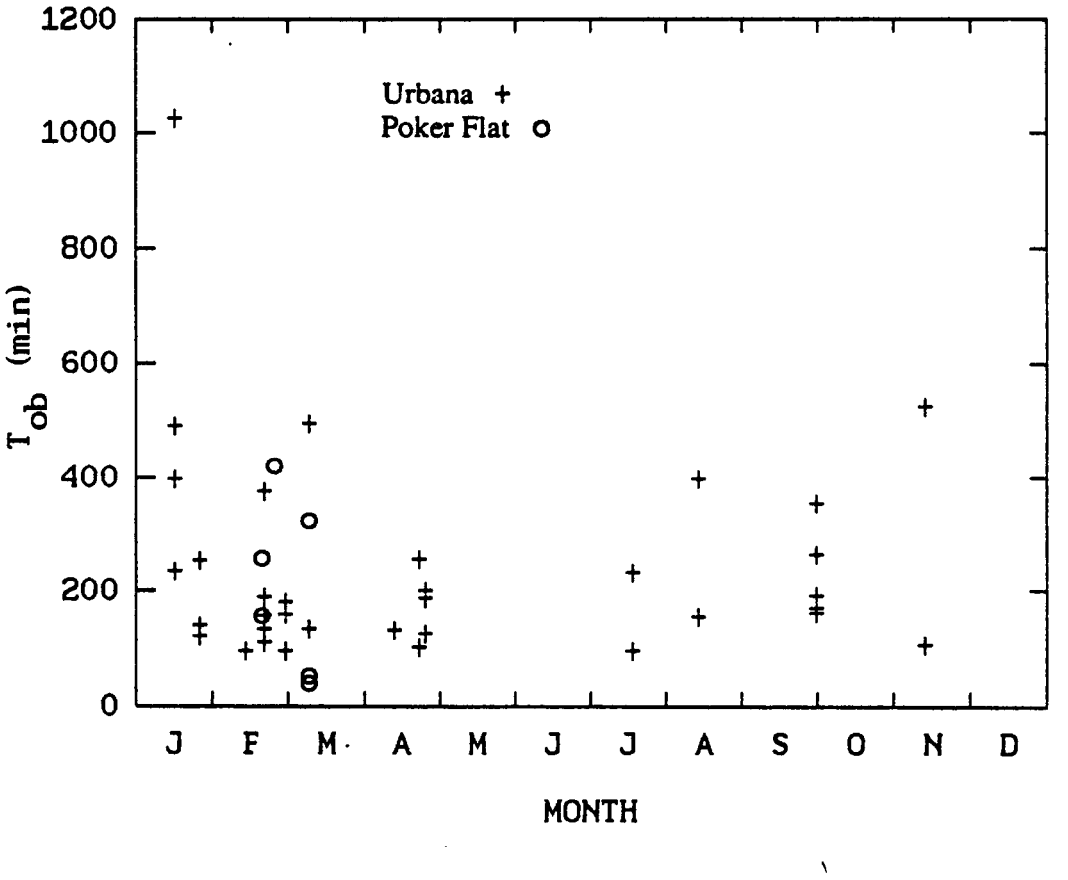

Figure 15. Seasonal distribution of observed wave periods.

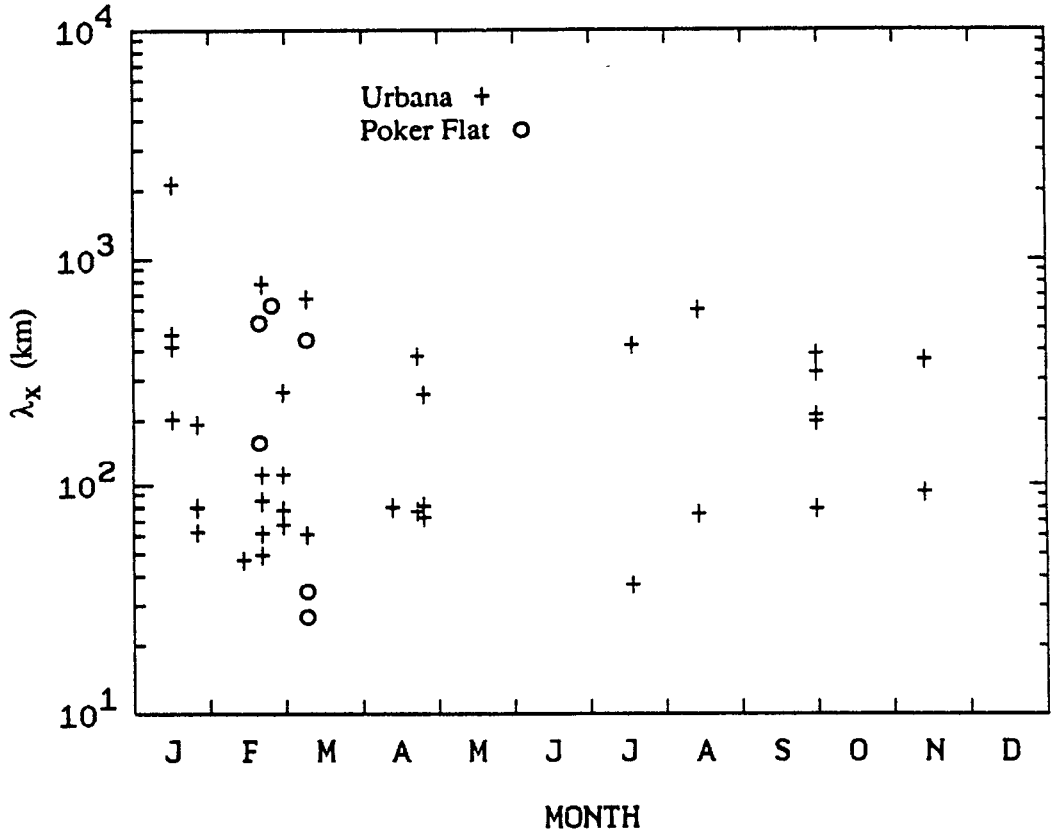

Figure 16. Seasonal distribution of horizontal wavelengths.

The amplitude of each wave event at the mid-altitude point of the observation range is determined by measuring the energy density at the spectral peak and applying Eq. (21). The seasonal distributions of wave amplitudes are illustrated in Figure 17. Most of the calculated wave amplitudes ranged from 1 to 5 %. The amplitudes of monochromatic wave events measured near the mesopause with sodium lidar were usually 1 to 5 % with maximum values ranging up to 17 % [Gardner and Voelz, 1987].

Atmospheric scale heights were computed for each observation date from the average photocount profile for the evening's observations. Seasonal distributions of atmospheric scale heights are shown in Figure 18. Measured scale heights ranged from 6.5 to 7.6 km with a median value of 7 km. The standard atmosphere specifies H to be approximately 7 km at an altitude of 35 km. Atmospheric scale heights determined from our data appear to be greater in spring and summer months.

The range of wave parameters measured in this study is consistent with previous measurements of gravity wave parameters obtained using a wide variety of observation techniques. Dominant vertical wavelengths near 2-4 km and 7 -10 km appear evident from both the relative occurrence of wave events and Fourier analysis of the data. Shibata et al. [1986] appear to have averaged photocount data over altitude to obtain a 1.5 km range bin resolution, and the data presented by Chanin and Hauchecorne [1981] were smoothed over 3.3 km, precluding observations of short wavelength events. Values of c_z measured in this study appear larger than what is typically observed in the same altitude region by the other two Rayleigh lidar studies. No seasonal variations of gravity wave activity are apparent from the wave parameters reported in this study, with the exception of a possible trend to shorter wave periods in the summer. More observations in the summer months are needed to clarify seasonal activity. Our values of c_z in winter are clearly greater than zero, in constrast to the near zero values reported by Shibata et al. [1986].

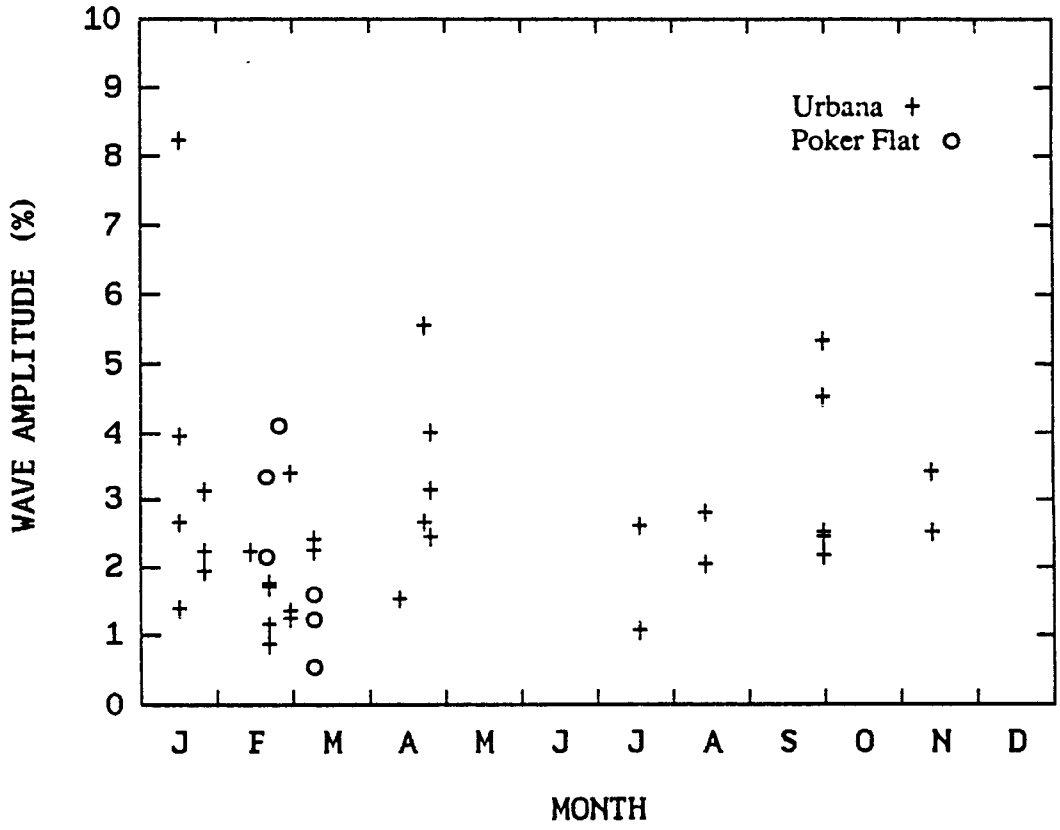

Figure 17. Seasonal distribution of wave amplitudes.

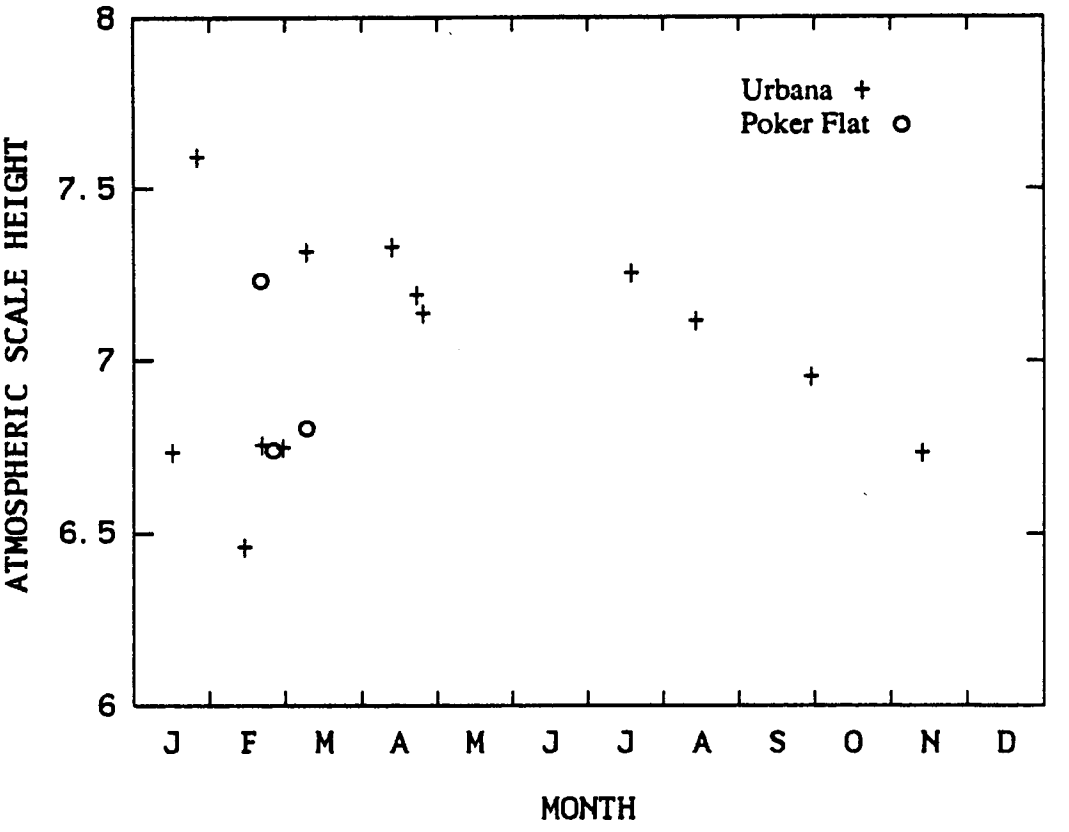

Figure 18. Seasonal distribution of atmospheric scale heights.

6. RELATIONSHIPS BETWEEN GRAVITY WAVE PARAMETERS

The vertical phase velocity is plotted versus vertical wavelength in Figure 19. There is considerable scatter in the data presented here. A regression curve of the form $c_z = C(\lambda_z)^p$ where C is the coefficient and p is the slope has been fitted to the data. Since c_z and λ_z are measured parameters, and consequently, both contain errors, the maximum likelihood (ML) regression algorithm described in Voelz and Gardner [1986] was used to estimate the power law fit for the data presented in this figure. This method assumes measurement errors in the dependent (c_z) and independent (λ_z) parameters are statistically independent and Gaussian distributed. The ML power law relation obtained from the data is plotted in Figure 19. The power law relation deduced from the sodium lidar data is plotted as a dashed line [Gardner and Voelz, 1987]. The correlation between c_z and λ_z is very low (0.089) in our Rayleigh data. Events with wavelengths near 2-3 km generally had 0.3 m/s phase velocities when observed with 60-minute measurement periods. However, two wave events with short wavelengths and large phase velocities were observed in the Poker Flat data using 20-minute integration periods. Shorter vertical wavelengths (2-3 km) that were observed near the mesopause with sodium lidar were associated with phase velocities near 1 m/s, while the longer wavelength (7-10 km) events corresponded to lower phase velocities. Sodium lidar measurements were taken using 10-minute integration periods. The relationship between λ_z and c_z determined with sodium lidar observations was not evident in the Urbana Rayleigh scatter data using 60-minute integration times. This is expected, since wave events with 30- to 50-minute periods will be averaged out with integration periods of 60 minutes. Neither Chanin and Hauchecorne [1981] nor Shibata et al. [1986] observed large phase velocities in this altitude region with 20-minute integration periods.

Both vertical and horizontal wavelengths show a strong tendency to increase with increasing periods and are plotted versus the observed period for each wave event in Figures 20 and 21. The higher correlation of the data presented in Figure 21 can be partially attributed to the manner in which λ_x is computed [Gardner and Voelz, 1987]. Sodium lidar studies of monochromatic wave activity also indicate that λ_z and λ_x tend to increase with increasing values of T_{ob} [Gardner and Voelz, 1987]. The power law curves for the sodium data are plotted as dashed lines in Figures 20 and 21.

Vertical phase velocity is shown as a function of the observed wave period in Figure 22. The power law curve determined from the Rayleigh data is also indicated. The relationship between c_z and T_{ob} found with sodium lidar gravity wave measurements is illustrated in this figure with a dashed line [Gardner and Voelz, 1987].

Kinetic energy is calculated for each monochromatic wave event at the mid-altitude point of the observation range using Eq. (21). The estimated kinetic energy is plotted versus the vertical wavenumber $k_z/2\pi$ in Figure 23. Much of the scatter evident here can be attributed to errors due

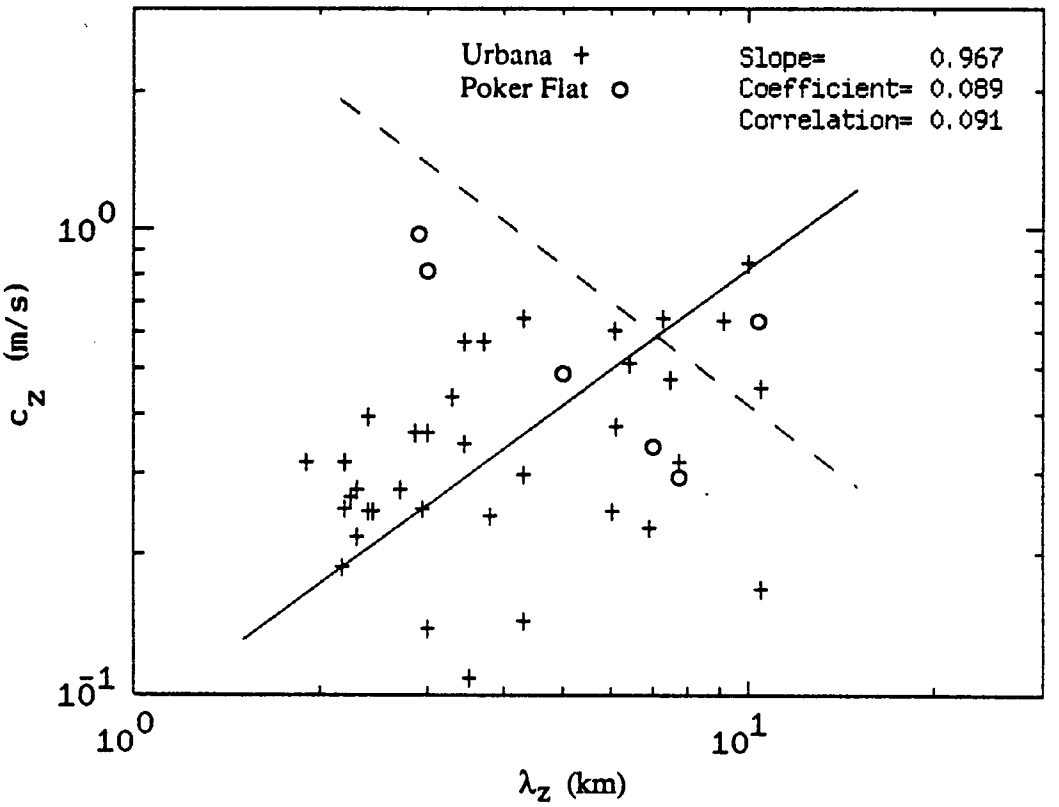

Figure 19. Vertical phase velocity versus vertical wavelength. The solid line is the ML power law fit of the form $c_z = C(\lambda_z)^p$ where p is the slope and C is the coefficient. The power law fit $c_z = 4.09(\lambda_z)^{-0.99}$ obtained with sodium lidar observations is indicated with a dashed line [Gardner and Voelz, 1987].

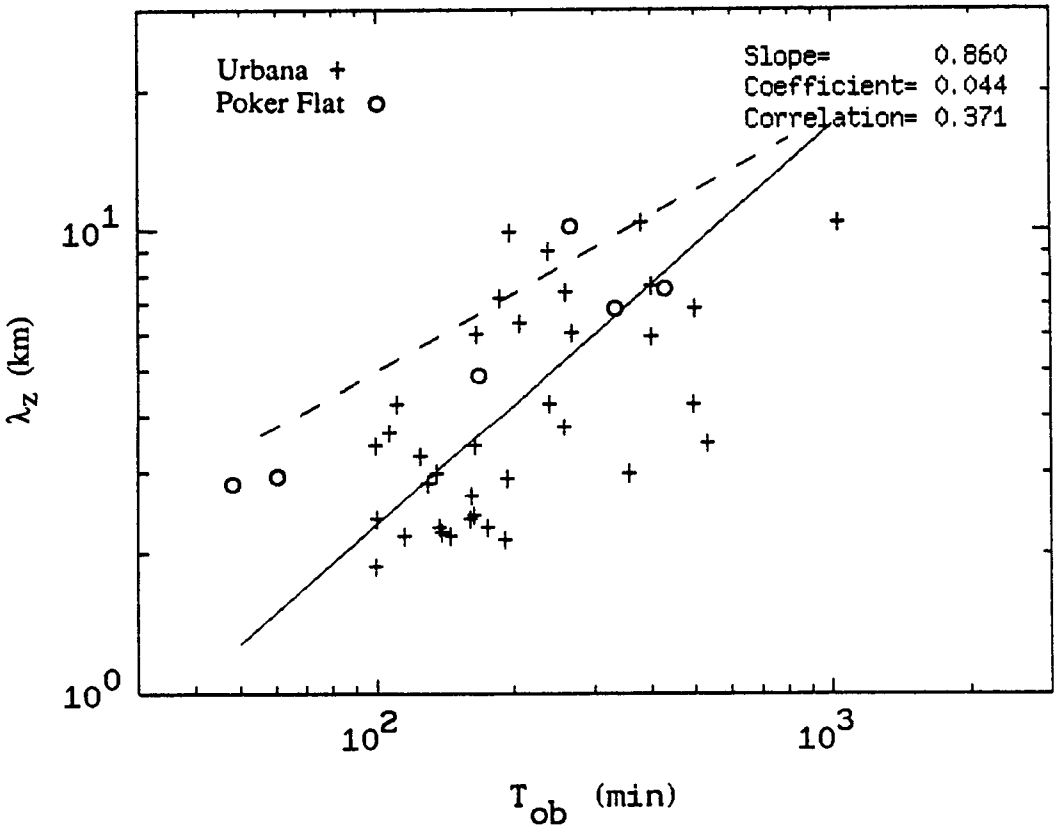

Figure 20. Vertical wavelength versus observed wave period. The solid line is the ML power law fit of the form $\lambda_z = C(T_{ob})^p$ where p is the slope and C is the coefficient. The power law fit $\lambda_z = 0.4(T_{ob})^{-0.55}$ obtained with sodium lidar observations is indicated with a dashed line [Gardner and Voelz, 1987].

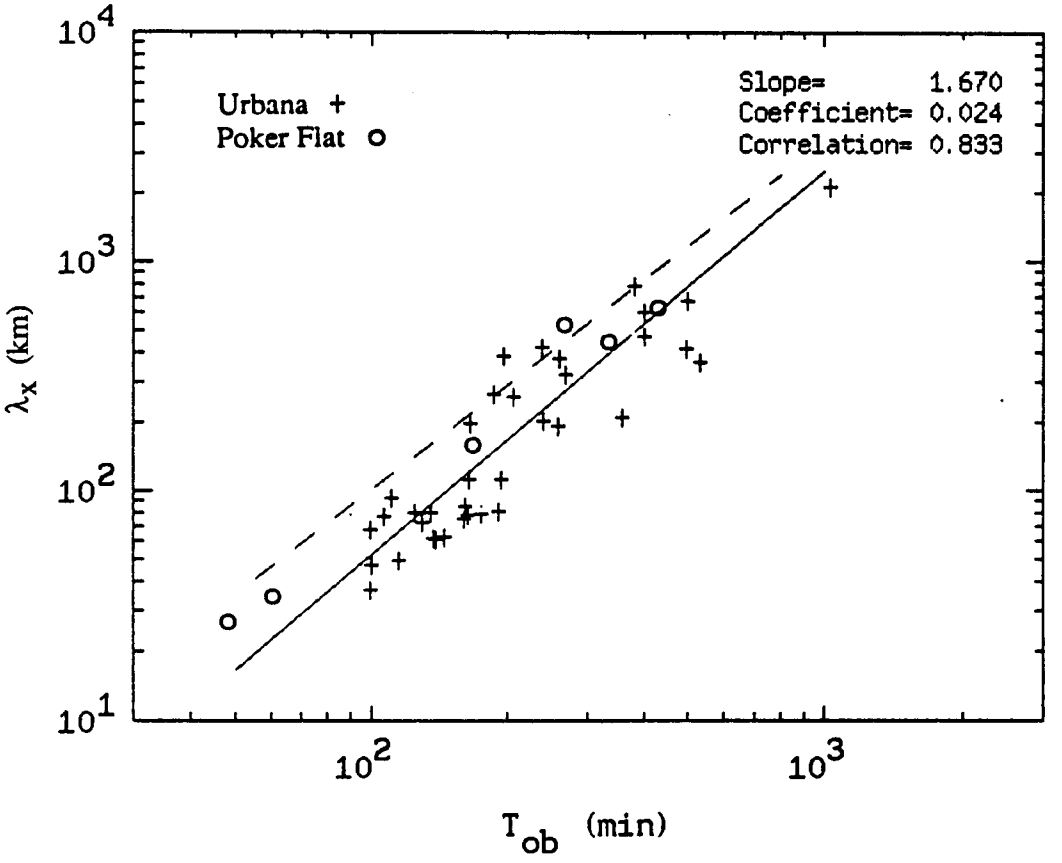

Figure 21. Horizontal wavelength versus observed wave period. The solid line is the ML power law fit of the form $\lambda_x = C(T_{ob})^p$ where p is the slope and C is the coefficient. The power law fit $\lambda_x = 0.093(T_{ob})^{1.52}$ obtained with sodium lidar observations is indicated with a dashed line [Gardner and Voelz, 1987].

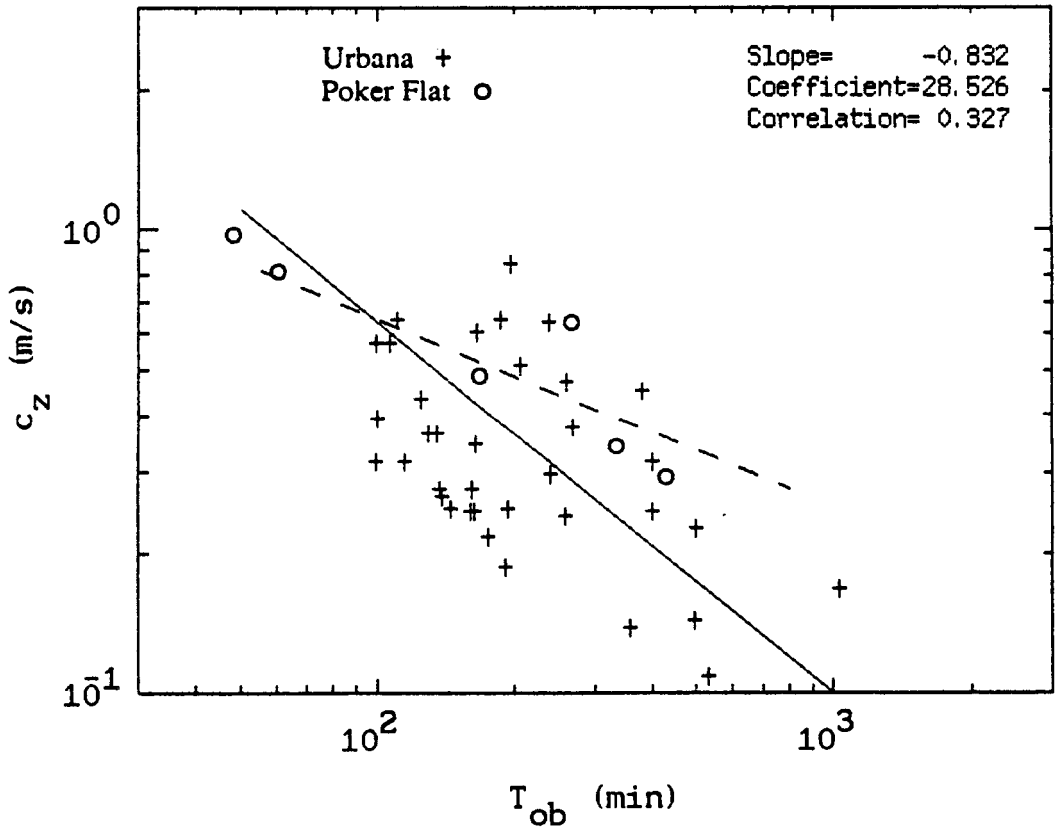

Figure 22. Vertical phase velocity versus observed wave period. The solid line is the ML power law fit of the form $c_z = C(T_{ob})^p$ where p is the slope and C is the coefficient. The power law fit $c_z = 10.2(T_{ob})^{-0.54}$ obtained with sodium lidar observations is indicated with a dashed line [Gardner and Voelz, 1987].

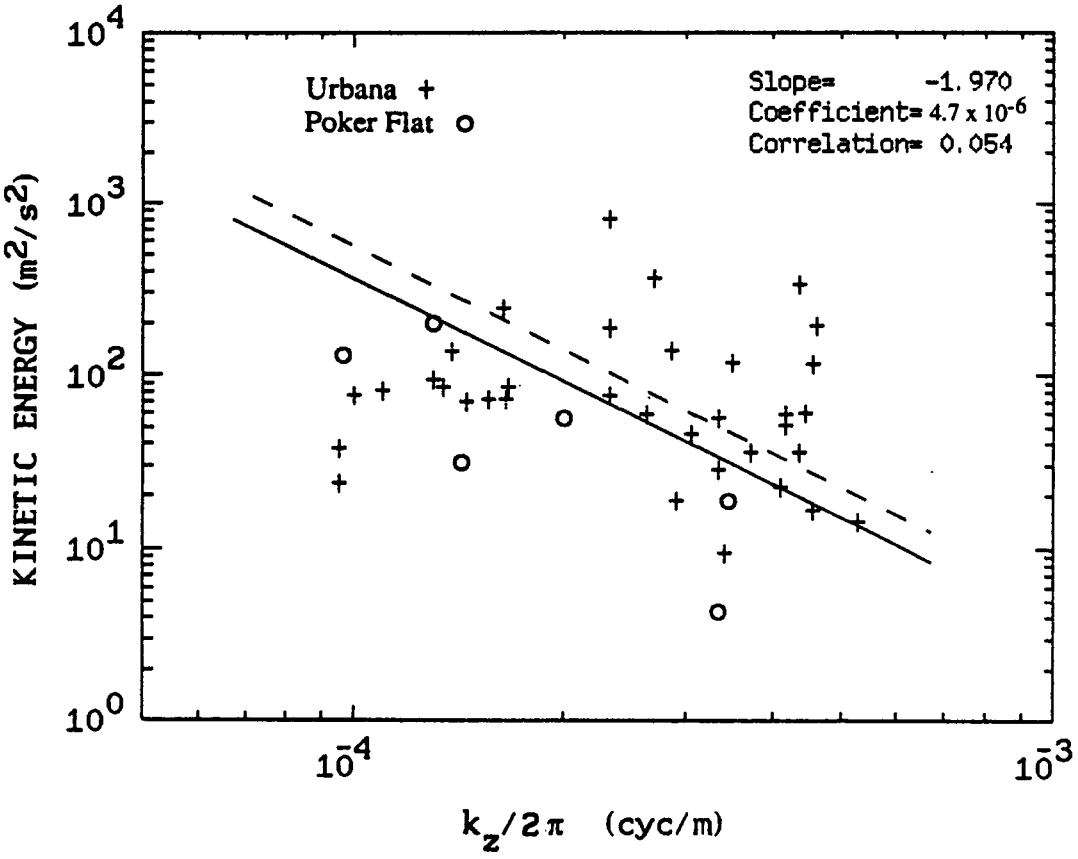

Figure 23. Kinetic energy versus vertical wavenumber. The solid line is the ML power law fit of the form $KE = C(k_z)^p$ where p is the slope and C is the coefficient. The kinetic energy dependence predicted by the linear saturation theory is shown in the dashed line [Gardner andVoelz, 1987].

to shot noise. Although the scatter is significant, the ML power law estimates from the data suggest a k_z^{-2} dependence of kinetic energy. The distribution shown here can be compared with the vertical wavenumber dependence of kinetic energy predicted by the linear saturation theory [Dewan and Good, 1986]. A monochromatic wave is expected to become saturated when its amplitude growth reaches the point of convective instability. This implies that at saturation conditions the horizontal perturbation velocity is equal to the intrinsic horizontal phase speed of the wave,

$$\left|v_x\right|_{sat} = c_{ix} = c_x - v_o = \frac{\lambda_x}{T} = \frac{\lambda_z}{T_{BV}} \quad , \tag{27}$$

where v_o is the mean background wind velocity and T is the intrinsic period of the wave. The KE distribution predicted by saturation theory is then obtained from Eq. (19),

$$KE_{sat} = \frac{\lambda_z^2}{2T_{BV}^2} = \frac{N^2}{2k_z^2} \quad . \tag{28}$$

The dashed line in Figure 23 is the predicted distribution of KE_{sat}. Most of the data points at vertical wavelengths greater than 5 km fall below this line. The distribution of kinetic energies observed in sodium lidar studies near the mesopause followed a k_z^{-3} dependence [Gardner and Voelz, 1987].

Kinetic energy is plotted as a function of the horizontal wavenumber $k_x/2\pi$ and observed frequency f_{ob} for each monochromatic wave event in Figures 24 and 25. The power law fits obtained from the Rayleigh lidar data are illustrated with a solid line and indicate a k_x^{-1} and $f_{ob}^{-1.7}$ dependence. The kinetic energy distributions for the sodium lidar data are shown with dashed lines in Figures 24 and 25. [Gardner and Voelz, 1987].

The correlation coefficients for the Rayleigh data power law relationships were usually less than 0.3. Sodium lidar measurements produced higher correlation, ranging between 0.5 and 0.9 [Gardner and Voelz, 1987]. The significant scatter in our Rayleigh data could be attributed to the quality of the data or simply the absence of dominant relationships between the gravity wave parameters. Short wave periods associated with smaller vertical wavelengths were not observed in the Urbana Rayleigh lidar data using 60-minute integration periods. Vertical and horizontal wavelengths increase with increasing periods in both lidar observations. Meek et al. [1985] also computed power law relations for λ_z and λ_x versus T and T_{ob}. A comparison of wave parameter relationships obtained from the Rayleigh lidar data, sodium lidar [Gardner and Voelz, 1987], and radar studies [Meek et al., 1985] is shown in Table 2. The differences between the observed relationships are probably the result of the particular measurement biases, resolutions, and accuracies that are inherent in each system.

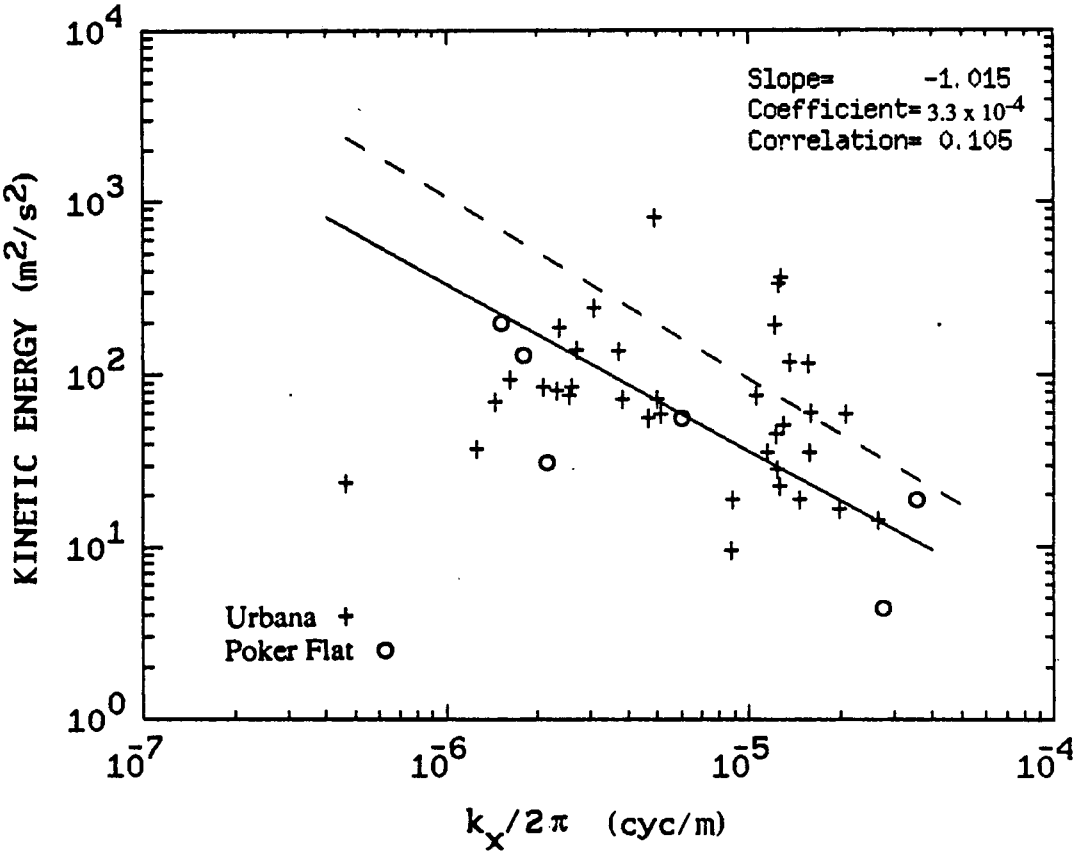

Figure 24. Kinetic energy versus horizontal wavenumber. The solid line is the ML power law fit of the form $KE = C(k_x)^p$ where p is the slope and C is the coefficient. The power law fit $KE = 5.3 \times 10^{-4}(k_x)^{-1.05}$ obtained with sodium lidar observations is indicated with a dashed line [Gardner and Voelz, 1987].

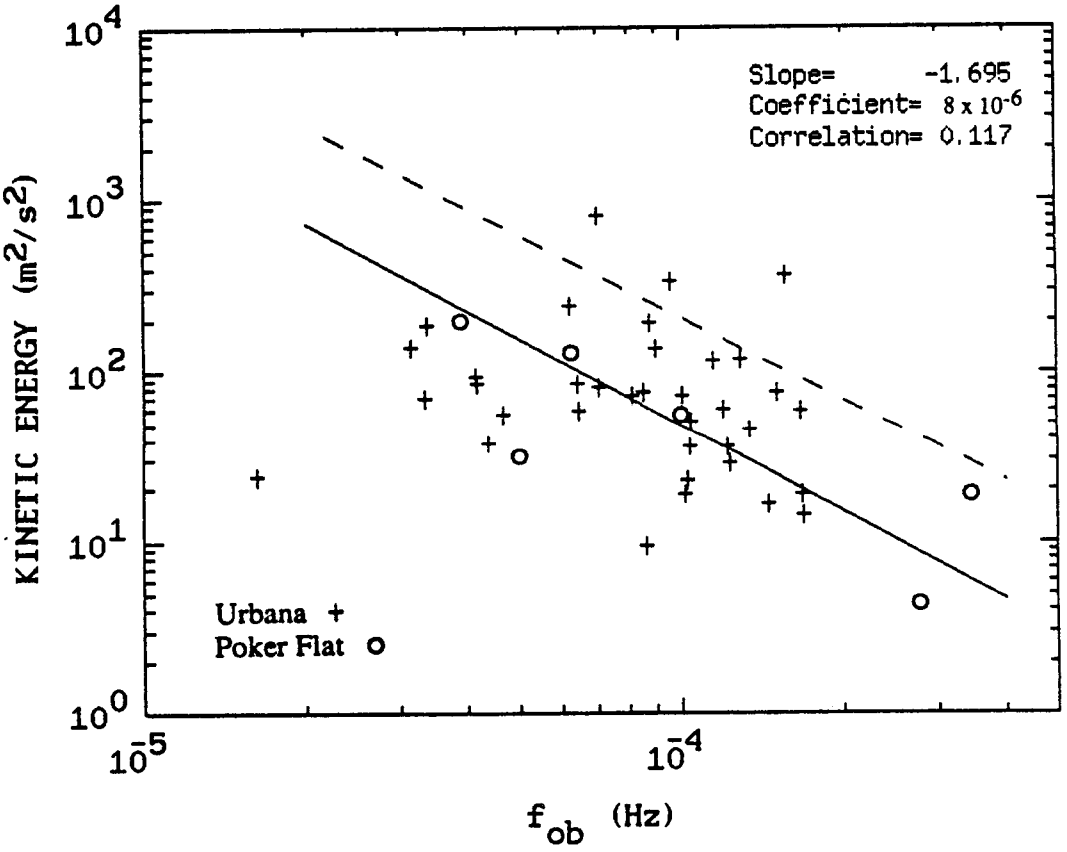

Figure 25. Kinetic energy versus observed wave period. The solid line is the ML power law fit of the form $KE = C(f_{ob})^p$ where p is the slope and C is the coefficient. The power law fit $KE = 9 \times 10^{-5}(f_{ob})^{-1.59}$ obtained with sodium lidar observations is indicated with a dashed line [Gardner and Voelz, 1987].

TABLE 2. Comparison of Rayleigh Lidar, Sodium Lidar and Radar Measurements of Power Law Relationships Between λ_z, λ_x, c_z, T_{ob}, T , and KE

	Rayleigh Lidar Data[1]	Sodium Lidar Data[2]	MF Radar Data[3]
Altitude Range	25-55 km	80-105 km	60-110 km
c_z vs λ_z	$c_z = 0.089(\lambda_z)^{0.886}$	$c_z = 4.09(\lambda_z)^{-0.99}$	
λ_z vs T_{ob}	$\lambda_z = 0.044(T_{ob})^{0.958}$	$\lambda_z = 0.4(T_{ob})^{0.55}$	$\lambda_z = 172(T)^{-0.73}$
λ_x vs T_{ob}	$\lambda_x = 0.024(T_{ob})^{1.765}$	$\lambda_x = 0.093(T_{ob})^{1.52}$	$\lambda_x = 9(T_{ob})^{0.68}$
			$\lambda_x = 39(T)^{0.24}$
c_z vs T_{ob}	$c_z = 28.5(T_{ob})^{-0.85}$	$c_z = 10.2(T_{ob})^{-0.54}$	
KE vs k_z	$KE = 4 \times 10^{-6}(k_z)^{-1.96}$	$KE = 1.1 \times 10^{-9}(k_z)^{-2.95}$	
KE vs k_x	$KE = 3.3 \times 10^{-4}(k_z)^{-1}$	$KE = 5.3 \times 10^{-4}(k_z)^{-1.05}$	
KE vs f_{ob}	$KE = 8 \times 10^{-6}(k_z)^{-1.68}$	$KE = 9 \times 10^{-5}(k_z)^{-1.59}$	

[1] This paper

[2] Gardner and Voelz, 1987

[3] Meek et al., 1985

7. ALTITUDE PROFILES OF WIND VELOCITY AND KINETIC ENERGY DENSITY

The mean-square velocity perturbations as a function of altitude provide a quantitative indication of gravity wave activity and limiting processes in the atmosphere. A profile of velocity versus altitude can be calculated by scaling the temporal mean-square density perturbation values

$$< v_x^2(z) > = \left(\frac{\gamma H N}{\gamma - 1}\right)^2 < r^2(z) > \approx \left(\frac{\gamma H N}{\gamma - 1}\right)^2 \frac{1}{T} \int_{t_o}^{t_o + T} r^2(z, t)\, dt \qquad (29)$$

where T is the duration of observation. An altitude profile of rms wind velocities for Urbana observations on March 8, 1984 is illustrated in Figure 26. Each 60-minute density perturbation profile is first spatially low-pass filtered using a cutoff wavelength of 5 km to reduce shot noise contamination. The mean-square density perturbation over the evening is computed for each range bin and scaled by $[\gamma HN/(\gamma - 1)]^2$. The oscillations in the data seem to indicate the presence of a stationary wave with period longer than the duration of the evening's observations. The range of rms velocities is 1 to 4 m/s. Wave amplitude clearly grows with altitude, but the wide oscillations make it difficult to reliably extract a growth length.

These oscillations can be integrated out by computing the mean-square wind velocity over more observation dates. The rms wind profile from 35-50 km for eight Urbana data sets is presented in Figure 27. Again, only a portion of the Urbana data can be utilized due to differences in observation altitude. Averaged velocity perturbations increase with altitude with values near 1.75 m/s at 35 km to 3.5 m/s at 50 km. Since the data were low-pass filtered, only gravity wave activity corresponding to wavelengths greater than 5 km is included. The average amplitude growth length for the altitude profile of rms wind perturbation is 20.9 km. The July 17, 1984 observations included in this average showed no amplitude growth in rms velocity. The velocity amplitudes of gravity waves in an isothermal atmosphere are expected to grow exponentially with height as $e^{z/2H}$, in order to conserve kinetic energy. The theoretical growth length for unsaturated waves in this altitude region is $2H \cong 14$ km. Since the measured growth length for the Rayleigh lidar observations is longer than the theoretical growth length, we can infer that waves propagating in this altitude region are, on the average, subject to effects that limit the amplitude growth rate. Amplitude growth lengths ranging from 10 to 100 km with a mean value of 19 km were measured for monochromatic gravity wave events observed in the sodium layer [Gardner and Voelz, 1987]. Sodium lidar observations of the rms wind perturbations at Urbana also show an 18 km amplitude growth length [Senft et al., 1987]. The wind velocities plotted in Figure 27 can be extrapolated to a value approaching 20 m/s near 85 km by using the measured amplitude growth length of 21 km. Velocity perturbations of 20 m/s are comparable to values obtained from sodium lidar measurements [Senft et al., 1987].

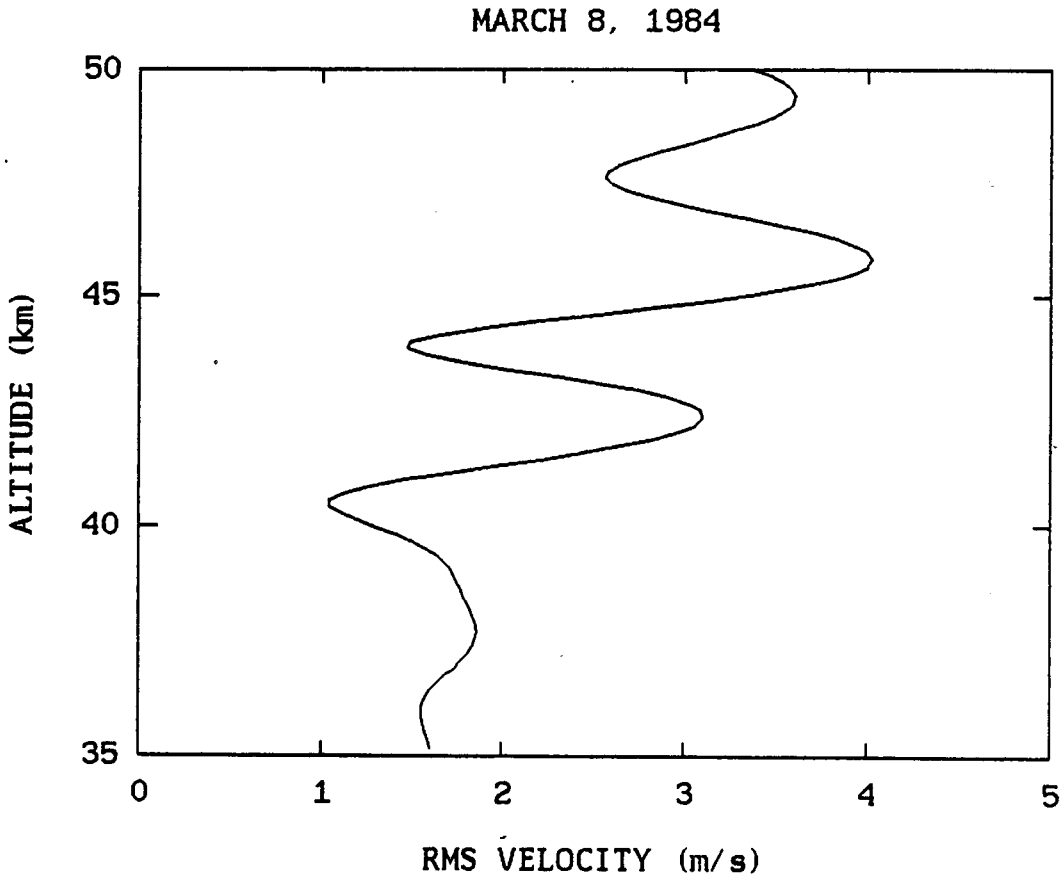

Figure 26. Altitude variations of rms wind perturbations for March 8, 1984 Urbana data. Each 60-minute density perturbation profile was spatially low-pass filtered using a cutoff wavelength of 5 km.

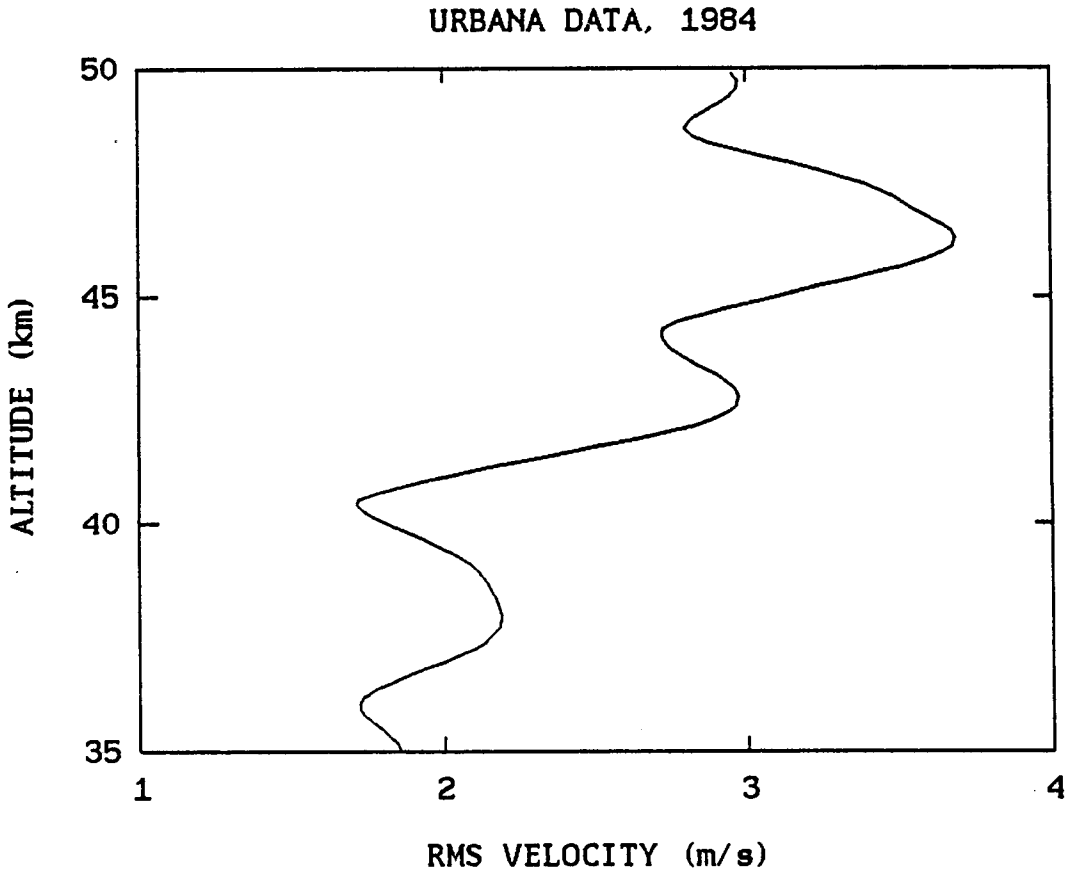

Figure 27. Altitude variations of rms wind perturbations averaged over eight Urbana observation nights. Each 60-minute density perturbation profile was spatially low-pass filtered using a cutoff wavelength of 5 km.

Both dissipation and saturation processes will attenuate gravity waves as they propagate upward in the atmosphere. Dissipation processes are independent of wave amplitude, while saturation depends upon wave amplitude. To illustrate that waves observed in this study are not propagating upward at unsaturated growth rates, we compute the altitude profile of kinetic energy density from mean-square velocity perturbations using

$$KE(z) = \frac{\rho(z)}{2} < v_x^2(z) > \qquad (30)$$

where the atmospheric density $\rho(z)$ is obtained by referencing photocount data to the standard atmosphere at 35 km. The average kinetic energy density profile computed from eight Urbana observation nights is shown in Figure 28. Kinetic energy clearly decreases with altitude. Decreasing kinetic energy with increasing height indicates that either (1) wave energy is being dissipated or saturated as waves propagate upward or (2) waves are propagating upward through vertical gradients in the mean background wind flow [Balsley and Garello, 1985; Vincent and Fritts, 1987]. The scale height for the KE profile plotted in Figure 28 was 18.2 km. Vincent and Fritts [1987] calculated kinetic energy scale heights in the 60-110 km altitude region with a MF radar and obtained values ranging from 8.6 to 16.2 km. The kinetic energy density profile shown in Figure 28 is similar to the KE density profile obtained by Balsley and Garello [1985] with the Poker Flat MST radar. The Poker Flat radar was used to measure the mean-square horizontal wind perturbations (E-W direction) at altitudes below 25 km and above 60 km. A kinetic energy profile from 25-60 km can be inferred from the MST radar observations at lower and higher altitudes [Balsley and Garello, 1985]. In the 25-60 km echo gap altitude region the kinetic energy scale height was estimated to exceed 10 km. The inferred KE profile is greater than our KE profile in the 35-50 km altitude region by about a factor of two. This difference could become even greater if we account for less dominant N-S winds. The rms winds computed from the MST radar KE profile are approximately 8 m/s at 60 km and 1.4 m/s at 25 km. The rms velocities measured with Rayleigh lidar in the 35-50 km altitude region are within these bounds.

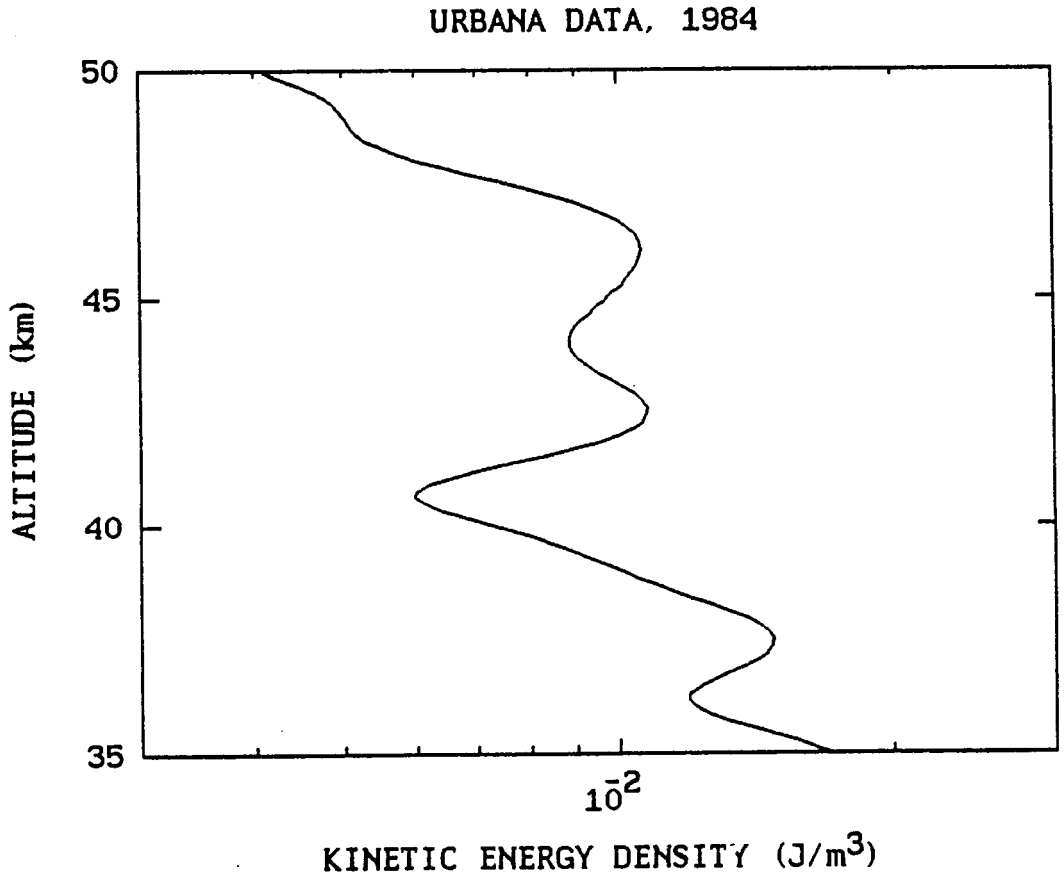

Figure 28. Altitude profile of kinetic energy density computed from rms wind perturbation data averaged over eight Urbana observation nights.

8. CONCLUSIONS

Rayleigh lidar is an effective tool to observe the dynamics of the atmosphere at altitudes inaccessible to radar measurements. The propagation of monochromatic gravity waves can be observed by examining altitude profiles of density perturbation and the vertical wavenumber spectrum of the horizontal winds. The data examined in this study suggest that substantial gravity wave activity is present in the 25-55 km altitude region. Forty-two monochromatic wave events were identified and characterized in 16 observation nights. Significant features of the data are the dominant vertical wavelengths between 2-4 km and 7-10 km and the tendency for both vertical and horizontal wavelengths to increase with an increasing wave period. The data integration period determines the range of the monochromatic wave temporal frequency spectrum which will be evident in the spatial profiles. A comparison of observations with 20- and 60-minute integration periods indicates that monochromatic wave activity is present in a broad range of the temporal frequency spectrum. The kinetic energy distribution approximates the k_z^{-2} dependence predicted by the linear saturation theory. Altitude profiles of rms wind velocity and kinetic energy also suggest that saturation or dissipation effects are limiting the growth of wave amplitudes.

The quality of the data used in this study is relatively poor in comparison to data obtainable with a wavelength-optimized Rayleigh lidar based on currently available technology. The temporal and spatial resolutions of the data presented here are inadequate to precisely characterize the entire spectrum of monochromatic wave behavior. Nevertheless, these measurements are important due to lack of observational data at these altitudes. The data analysis techniques and results illustrated here demonstrate the potential of Rayleigh scatter lidar.

APPENDIX A: RAYLEIGH LIDAR PERFORMANCE EVALUATION

In this appendix we derive the equations necessary to evaluate the performance of Rayleigh scatter lidar systems. The critical measure of lidar performance is the spatial and temporal resolution. Shot noise contaminates the data and limits the resolution of gravity wave measurements. The data processing tradeoffs between integration time, observation range and vertical wavelength resolution are described.

The photocount in a Rayleigh lidar system is proportional to atmospheric density and inversely proportional to the square of the range. The expected Rayleigh scatter photocount in the absence of wave perturbations can be modeled as

$$< N(z) > = \frac{z_o^2 N_o}{z^2} \frac{\rho(z)}{\rho(z_o)} \approx \frac{z_o^2 N_o}{z^2} e^{-(z - z_o)/H} \qquad \text{(A1)}$$

where N(z) is the measured signal photocount and N_o is the expected photocount at the lower altitude z_o. Because the Rayleigh scatter photocounts decay exponentially with altitude, N_o will clearly be larger at lower altitudes. The atmospheric density is estimated from the measured photocount by range scaling and multiplying by an appropriate scaling constant ξ,

$$\rho(z) = \xi z^2 N(z) \; . \qquad \text{(A2)}$$

By substituting Eq. (A2) into Eq. (23) the measured value of r(z) becomes

$$r(z) \approx \frac{\xi z^2 N(z)}{\rho_o(z)} - 1 \; . \qquad \text{(A3)}$$

The discrete Fourier transform of r(z) is given by

$$R(k_z) = \sum_m \left[\frac{\xi (m\Delta z)^2 N(m\Delta z)}{\rho_o(m\Delta z)} - 1 \right] e^{i k_z m \Delta z} \Delta z \qquad \text{(A4)}$$

where Δz is the reciever range gate width. The expected power spectrum is obtained from the magnitude squared of the discrete Fourier transform,

$$< \left| R(k_z) \right|^2 > = \sum_m \sum_l < \left[\frac{\xi (m\Delta z)^2 N(m\Delta z)}{\rho_o(m\Delta z)} - 1 \right] \left[\frac{\xi (l\Delta z)^2 N(l\Delta z)}{\rho_o(l\Delta z)} - 1 \right] > e^{i k_z (m - l) \Delta z} \Delta z. \qquad \text{(A5)}$$

Because $N(m\Delta z)$ is a Poisson process, the photocount fluctuations will introduce shot noise into the calculated values of $| R(k_z) |^2$. Equation (A5) can be simplified by noting

$$< N(m\Delta z)\, N(l\Delta z) > = \begin{cases} <N_m><N_l> & m \neq l \\ <N_m>^2 + <N_m> & m = l \end{cases} , \qquad \text{(A6)}$$

so that

$$< \left| R(k_z) \right|^2 > = \left| \sum_m \left[\frac{\xi\,(m\Delta z)^2 <N(m\Delta z)>}{\rho_o(m\Delta z)} - 1 \right] e^{i k_z m\Delta z}\, \Delta z \right|^2$$

$$+ \sum_m \frac{\xi^2\,(m\Delta z)^2 <N(m\Delta z)>}{\rho_o^2(m\Delta z)}\, \Delta z^2 . \qquad \text{(A7)}$$

The first term in Eq. (A7) is the spectrum of the density perturbations while the second term is the shot noise floor.

The expression for the shot noise floor can be simplified by approximating the summation by an integral,

$$\sum_m \frac{\xi^2\,(m\,\Delta z)^4 < N_m >}{\rho_o^2\,(m\Delta z)}\, \Delta z^2 \approx \int_{z_o}^{z_o + L} \frac{z^2 \Delta z}{z_o^2 N_o}\, e^{(z - z_o)/H}\, dz$$

$$\approx \frac{\Delta z\, H}{N_o} \left(1 + \frac{L - H}{z_o} \right)^2 e^{L/H} . \qquad \text{(A8)}$$

We note that the shot noise level is inversely proportional to the photocount at z_o and grows exponentially with L, the altitude range of the observations. Equation (A8) clearly shows that the shot noise floor is decreased for observations at lower altitudes and over a limited range. By substituting Eq. (A8) into Eq. (A7) and scaling the result according to Eq. (10) we obtain an expression for the measured gravity wave spectrum

$$\frac{1}{2L} \left(\frac{\gamma H N}{\gamma - 1} \right)^2 < \left| R(k_z) \right|^2 > \approx E_x(k_z) + \frac{1}{2L} \left(\frac{\gamma H N}{\gamma - 1} \right)^2 \frac{\Delta z\, H}{N_o} \left(1 + \frac{L - H}{z_o} \right)^2 e^{L/H} . \qquad \text{(A9)}$$

It is more convenient to express the shot noise floor in terms of the total photocount comprising a profile

$$N_T = \sum_m < N(m\Delta z) > \approx \frac{z_o^2\, N_o}{\Delta z} \int_{z_o}^{z_o + L} \frac{e^{(z - z_o)/H}}{z^2}\, dz \approx \frac{N_o\, H}{\Delta z} . \qquad \text{(A10)}$$

By solving this equation for N_o and substituting the result into Eq. (A9) the measured gravity

wave spectrum becomes

$$\frac{1}{2L}\left(\frac{\gamma H N}{\gamma - 1}\right)^2 < \left| R(k_z) \right|^2 > \approx E_x(k_z) + \frac{1}{2L}\left(\frac{\gamma H N}{\gamma - 1}\right)^2 \frac{H^2}{N_T}\left(1 + \frac{L - H}{z_o}\right)^2 e^{L/H} . \tag{A11}$$

The theoretical spectrum for saturated gravity waves in the middle atmosphere [Dewan and Good, 1986; Smith et al.,1987],

$$E_x(k_z) = \frac{N^2}{2 k_z^3} . \tag{A12}$$

This expression can be used in Eq. (A11) to determine the range of vertical wavelengths where the energy density is greater than the noise floor,

$$\lambda_z > \left[\frac{8 \pi^3}{L N_T} \left(\frac{\gamma H^2}{\gamma - 1}\right)^2 \left(1 + \frac{L - H}{z_o}\right)^2 e^{L/H} \right]^{1/3} . \tag{A13}$$

Equation (A13) defines the spatial resolution of the Rayleigh scatter lidar. Shorter wavelengths can be observed by increasing the total photocount in a profile N_T or by decreasing the altitude range of observations L. The photocount return is enhanced by increasing the laser power, enlarging the receiver telescope area, or lengthening the measurement period.

The equations derived above can now be used to evaluate the expected performance of Rayleigh scatter measurements obtained with the AFGL and UIUC lidar systems. Since L and z_o are data processing parameters, N_T is the only variable in the above equations that is a function of system operating characteristics. The total signal photocount comprising a profile is computed using Eq. (A10) where N_o is determined from the Rayleigh lidar equation. The lidar equation calculates the expected number of backscattered photcounts from a laser directed into the atmosphere [Measures, 1977; Cerny and Sechrist, 1980]. The expected Rayleigh photocount per pulse from a scattering volume Δz thick centered at altitude z is given by

$$N(z) = \frac{\lambda E_L}{hc} \eta A_r T_a^2 \frac{\sigma_R n_A(z) \Delta z}{4 \pi z^2} \tag{A14}$$

where,

λ = laser operating wavelength;

E_L = laser energy per pulse;

h = Planck's constant (6.63×10^{-34} J-sec);

c = speed of light (3×10^{-8} m/sec);

A_r = effective receiver area (m^2);

T_a = one-way atmospheric transmittance (0.05);

σ_R = Rayleigh backscatter cross section (m^2);
$n_A(z)$ = atmospheric number density at altitude z;
Δz = range bin width (m).

The product of the Rayleigh backscatter cross section and atmospheric density can be expressed in terms of atmospheric pressure and temperature

$$\sigma_R\, n_A(z) = 3.54 \times 10^{-6}\, \frac{P}{T} \left(\frac{589}{\lambda(nm)} \right)^{4.0117} \qquad \text{(A15)}$$

where

P = atmospheric pressure (mbar);
T = atmospheric temperature (K).

By substituting Eq. (A15) into (A14) we obtain

$$N(z) = \frac{\lambda E_L}{hc} \frac{\eta A_r T_a^2}{4\pi z^2}\, 3.54 \times 10^{-6}\, \frac{P}{T} \left(\frac{589}{\lambda(nm)} \right)^{4.0117} \Delta z \qquad \text{(A16)}$$

Using the equations discussed above with the system parameters listed in Table 1 we can compute the shot noise floor and vertical wavelength resolution as a function of integration time for the AFGL and UIUC lidar systems.

The performance of the AFGL and UIUC lidar systems are evaluated for observations over the 35-50 km altitude range. The predicted shot noise floor is plotted as a function of integration time in Figure A.1. The shot noise floor for measurements with the AFGL Rayleigh lidar is approximately one-third lower than for measurements with the UIUC lidar. The noise floor for both lidars is clearly reduced with increased integration time. The vertical wavelength resolution based upon the model gravity wave spectrum is shown in Figure A.2. The expected spatial resolution with 60-minute measurement periods is better than 2 km for both lidars. Since the product of the system parameters $E_L A_r R$ is greater for the AFGL Rayleigh lidar, bettter resolution is possible.

Lidar systems designed to maximize Rayleigh backscatter returns would operate at wavelengths near 300 nm. Since photocounts have a λ^{-3} dependence, such lidar systems could expect an eight-fold increase in signal photocounts per profile. Significant gains in the signal-to-noise ratio and subsequent improvements in both the temporal and spatial resolutions could be realized with a laser pulse repetition rate of 250 Hz and a 250 nsec receiver range-gate width (37.5 m) that are possible in state-of-the-art lidars.

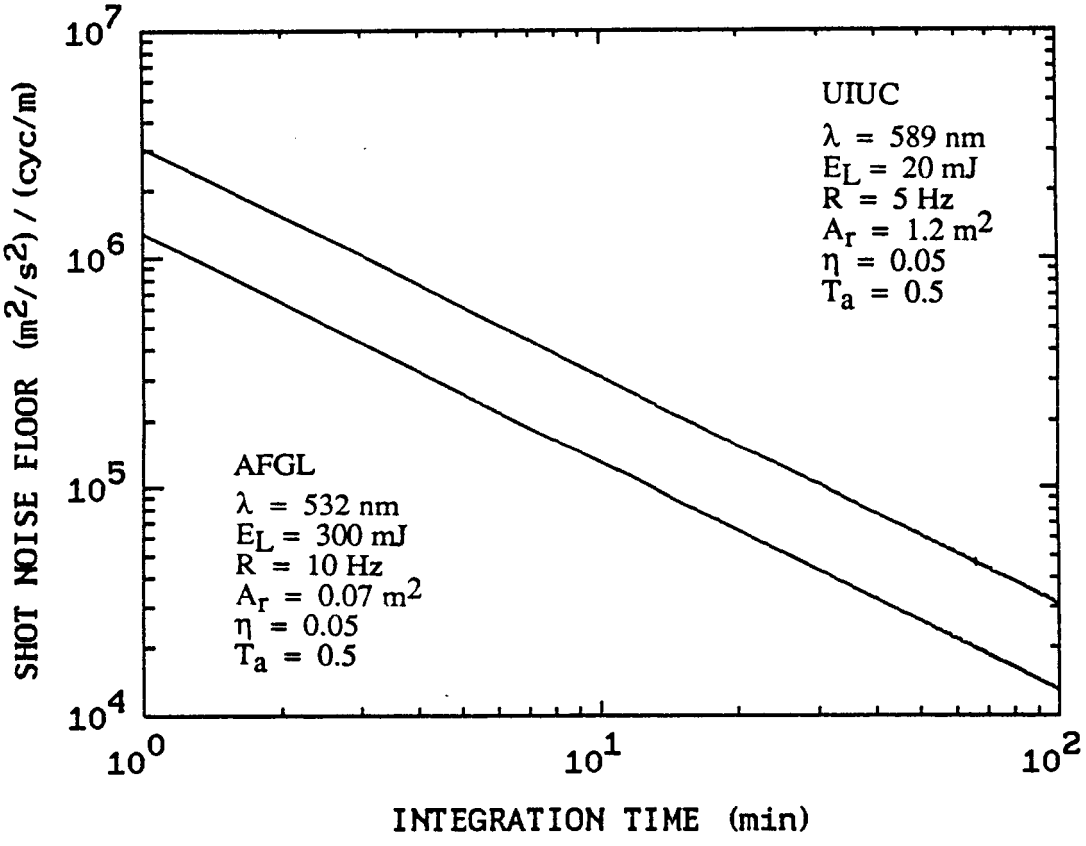

Figure A.1 Predicted shot noise floor as a function of integration time for observations over 35-50 km altitude range using the AFGL and UIUC lidar systems.

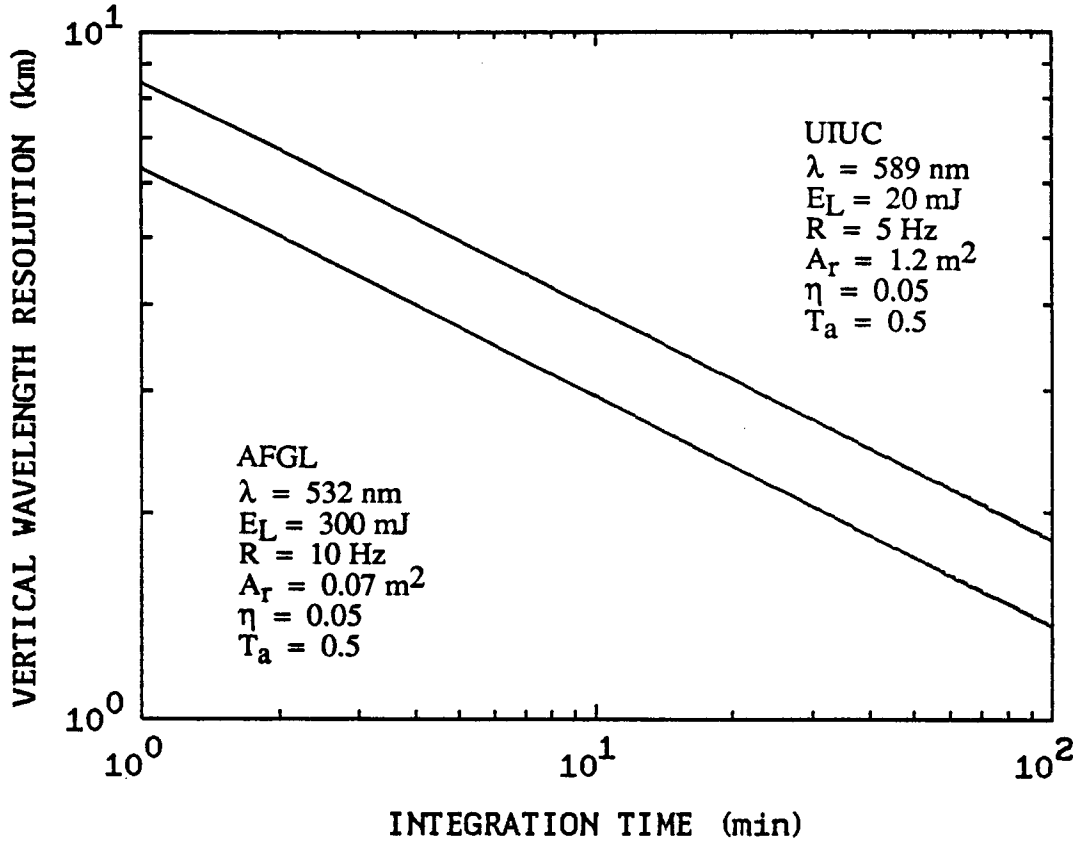

Figure A.2 Predicted vertical wavelength resolution as a function of integration time for observations over 35-50 km altitude range using the AFGL and UIUC lidar systems.

APPENDIX B: MEASURED GRAVITY WAVE PARAMETERS

1. AFGL Nd:YAG Rayleigh Lidar, Poker Flat, AK

Date	Obs. Range	Intg. Time	Cutoff (km)	λ_z (km)	c_z (m/s)	T_{ob} (min)	$Ae^{\beta z}$ (%)
Feb. 19, 1986	25-45 km	30 min	7.5	10.4	0.65	266	3.4
			3	5	0.5	167	2.22
Feb. 24, 1986	25-55 km	20 min	5	7.7	0.3	388	4.19
Mar. 8, 1986	25-45 km	20 min	5	7	0.35	333	1.66
	25-40 km	20 min	2.5	2.9	1.0	48	1.28
			2.5	3	0.83	60	0.62

2. UIUC Sodium Lidar, Urbana, IL

Date	Obs. Range	Intg. Time	Cutoff (km)	λ_z (km)	c_z (m/s)	T_{ob} (min)	$Ae^{\beta z}$ (%)
Jan. 15, 1986	30-42 km	60 min	7	10.5	0.17	1029	1.4
			5	6	0.25	400	4.0
			3.3	4.3	0.145	494	2.68
			3	4.3	0.3	239	8.25
Jan. 25, 1985	38-48 km	60 min	3	3.8	0.245	259	2.24
			2.5	3.28	0.44	124	3.14
			2	2.2	0.253	145	1.96
Feb. 13, 1984	30-40 km	60 min	2	2.4	0.4	100	2.25
Feb. 20, 1984	33-48 km	60 min	5	10.5	0.46	380	1.79
			2	2.7	0.28	161	1.74
			2	2.3	0.28	137	1.74
	33-45 km	60 min	2.5	2.94	0.253	194	0.89
			2	2.2	0.32	114	1.18
Feb. 29, 1984	35-50 km	60 min	6	7.25	0.65	186	3.42
			3	3.45	0.35	164	1.39
			3	3.45	0.58	99	1.27
			1.8	2.44	0.25	162	1.27
Mar. 8, 1984	35-50 km	60 min	5	6.9	0.23	500	2.43
			2	2.25	0.27	139	2.26
Apr. 12, 1985	35-50 km	30 min	2.75	3	0.37	135	1.55
Apr. 22, 1986	30-45 km	60 min	6	7.46	0.48	259	2.68
			3.3	3.7	0.58	106	5.59
Apr. 24, 1984	35-50 km	60 min	5	6.4	0.52	205	2.47
	35-47 km		2.5	2.86	0.37	129	3.16
			2	2.17	0.19	190	4.05
Jul. 17, 1984	35-50 km	60 min	7.5	9.1	0.64	237	2.62
			1.75	2	0.32	104	1.09
Aug. 13, 1984	35-50 km	60 min	5	8	0.32	417	2.83
	35-45 km		2	2.4	0.25	160	2.08
Sep. 30, 1984	35-50 km	60 min	8	11.5	0.85	225	2.53
			5	6.1	0.38	268	4.56
			5	6.06	0.61	165	5.37
			2.5	3	0.14	357	2.19
			2.5	2.3	0.22	174	2.47
Nov. 12, 1984	35-50 km	60 min	4	5	0.65	128	2.53
	35-45 km		3	3.5	0.11	530	3.43

LIST OF REFERENCES

Balsley, B. B., and R. Garello, The kinetic energy density in the troposphere, stratosphere and mesosphere: A preliminary study using the Poker Flat MST radar in Alaska, Radio Sci., 20, 1355-1361, 1985.

Balsley, B. B., and D. A. Carter, The spectrum of atmospheric velocity fluctuations at 8 and 86 km, Geophys. Res. Lett., 9, 465-468, 1982.

Cerny, T., and C. F. Sechrist, Jr., Calibration of the Urbana lidar system, Aeronomy Rep. No. 94, Aeronomy Laboratory, University of Illinois, Urbana, August 1980.

Chanin, M. L, Observation of the propagation and dispersion of gravity waves in the middle atmosphere, paper presented at Sixth International Symposium on Solar-Terrestrial Physics (SCOSTEP), Toulouse, France, 1986.

Chanin, M. L., Gravity wave study from Rayleigh lidar data, Int. Conf. Gravity Waves Turb. Mid. Atmos., Adelaide, May 20-23, 1987.

Chanin, M. L., and A. Hauchecorne, Lidar observation of gravity and tidal waves in the stratosphere and mesosphere, J. Geophys. Res., 86, 9715-9721, 1981.

Dewan, E. M., and R. E. Good, Saturation and the "universal" spectrum for vertical profiles of horizontal scalar winds in the atmosphere, J. Geophys. Res., 91, 2742-2748, 1986.

Fritts, D. C., Gravity wave saturation in the middle atmosphere: A review of theory and observations, Rev. Geophys., 22, 275-308,1984.

Gardner, C. S., and J. D. Shelton, Density response of neutral atmospheric layers to gravity wave perturbations, J. Geophys. Res., 90, 1745-1754, 1985.

Gardner, C. S., and D. G. Voelz, Lidar Measurements of gravity wave saturation effects in the sodium layer, Geophys. Res. Lett., 12, 765-768, 1985.

Gardner, C. S., and D. G. Voelz, Lidar studies of the nighttime sodium layer over Urbana, Illinois 2. Gravity Waves, J. Geophys. Res., 92, 4673-4694, 1987.

Gardner, C. S., D. G. Voelz, C. F. Sechrist, Jr. and A. C. Segal, Lidar studies of the nighttime sodium layer over Urbana, Illinois 1. Seasonal and nocturnal variations, J. Geophys. Res., 91, 13659-13673, 1986.

Hauchecorne, A., and M. L. Chanin, Density and temperature profiles obtained by lidar between 35 and 70 km, Geophys. Res. Lett., 7, 565-568, 1980.

Hines, C. O., Internal atmospheric gravity waves at ionospheric heights, Can. J. Phys., 38, 1441-1481, 1960.

Measures, R. M., Lidar equation analysis allowing for target lifetime, laser pulse duration, and detector integration period, Applied Optics, 16, 1092-1103, 1977.

Meek, C. E., I. M. Reid, and A. H. Manson, Observations of mesospheric wind velocities, 1. Gravity wave horizontal scales and phase velocities from spaced wind observations, Radio Sci., 20, 1363-1382, 1985.

Midgley, J. E., and H. B. Leimohn, Gravity waves in a realistic atmosphere, J. Geophys. Res., 71, 3729-3748, 1966.

Philbrick, C. R., D. P. Sipler, G. Davidson, and W. P. Moskowitz, Remote sensing of the structure of the middle atmosphere using lidar, Optical Society Topical Meeting on Laser and Optical Remote Sensing: Instrumentation and Techniques, 18, North Falmouth, MA, Sept. 28 - Oct. 1, 1987.

Richter, E. S., J. R. Rowlett, C. S. Gardner, and C. F. Sechrist, Jr., Lidar observations of the mesospheric sodium layer of Urbana, Illinois, J. Atmos. Terr. Phys., 43, 327-337, 1981.

Rowlett, J. R., C. S. Gardner, E. S. Richter, and C. F. Sechrist, Jr., Lidar observations of wavelike structure in the atmospheric sodium layer, Geophys. Res. Lett., 9, 683-686, 1978.

Senft, D., C. S. Gardner, and C. H. Liu, Na lidar measurements of the seasonal and nocturnal variations of the gravity wave vertical wavenumber spectra, Int. Conf. Gravity Waves Turb. Mid. Atmos., Adelaide, May 20-23, 1987.

Shelton, J. D., G. S. Gardner, and C. F. Sechrist, Jr., Density response of the mesospheric sodium layer to gravity wave perturbations, Geophys. Res. Lett., 7, 1069-1072, 1980.

Shibata, T., M. Kobuchi, and M. Maeda, Measurements of density and temperature profiles in the middle atmosphere with a XeF lidar, Applied Optics, 25, 686-688, 1986.

Shibata, T., T. Kukuda, and M. Maeda, Density fluctuations in the middle atmosphere over Fukuoka observed by an XeF Rayleigh lidar, Geophys. Res. Lett., 13, 1121-1124, 1986.

Smith S. A., D. C. Fritts, and T. E. VanZandt, Comparison of mesospheric wind spectra with a gravity wave model, Radio Sci., 20, 1331-1338, 1985.

Smith, S. A., D. C. Fritts, and T. E. VanZandt, Evidence for a saturated spectrum of atmospheric gravity waves, J. Atmos. Sci., 44, 1404-1410, 1987.

Vincent, R. A., and D. C. Fritts, A climatology of gravity wave motions in the mesopause region at Adelaide, Australia, J. Atmos. Sci., 44, 748-760, 1987.

Voelz, D. G., and C. S. Gardner, Theoretical and lidar studies of the seasonal and nocturnal variations of the mesospheric sodium layer at Urbana, Illinois, Rep. EOSL 86-006, Electro-Optic Systems Laboratory, University of Illinois, Urbana, December 1986.

CUMULATIVE LIST OF RADIO RESEARCH LABORTORY

AND ELECTRO-OPTIC SYSTEMS LABORTORY REPORTS

PREPARED UNDER NASA GRANT NSG-5049

RRL Rep. No. 469 - Gardner, C. S. and N. N. Rao (December 1975), The Effects of Random Path Fluctuations on the Accuracy of Laser Ranging Systems.

RRL Rep. No. 471 - Zanter, D. L., C. S. Gardner and N. N. Rao (January 1976), The Effects of Atmospheric Refraction on The Accuracy of Laser Ranging Systems.

RRL Rep. No. 477 - Gardner, C. S. and J. R. Rowlett (November 1976), Atmospheric Refraction Errors in Laser Ranging Data.

RRL Rep. No. 478 - Hendrickson, B. E. and C. S. Gardner (December 1976), Correction of Laser Ranging Data for the Effects of Horizontal Refractivity Gradients.

RRL Rep. No. 481 - Gardner, C. S. (February 1977), Statistics of the Residual Refraction Errors in Laser Ranging Data.

RRL Rep. No. 486 - Gardner, C. S. (July 1977), Comparison Between the Refraction Error Covariance Model and Ray Tracing.

RRL Rep. No. 488 - Gardner, C. S. (September 1977), Speckle Noise in Satellite Based Lidar Systems.

RRL Rep. No. 495 - Gardner, C. S. and G. S. Mecherle (April 1978), Speckle Noise in Direct-Detection Lidar Systems.

RRL Rep. No. 496 - Gardner, C. S. and A. M. Saleh (October 1978), Speckle Noise in Differential Absorption Lidar Systems.

RRL Rep. No. 499 - Gardner, C. S. (January 1979), A Technique for Remotely Measuring Surface Pressure from a Satellite Using a Multicolor Laser Ranging System.

RRL Rep. No. 502 - Palluch, E., J. D. Shelton and C. S. Gardner (May 1979), Operating Manual for the RRL 8 Channel Data Logger.

RRL Rep. No. 505 - Gardner, C. S. and R. Axford, Jr. (March 1980), Regression Models for Multicolor Satellite Laser Ranging.

RRL Rep. No. 510 - Gardner, C. S. (April 1981), Analysis of Target Signatures for Laser Altimeters.

RRL Rep. No. 511 - Gardner, C. S. (June 1981), Atmospheric Refraction Effects in Air Borne Laser Ranging.

RRL Rep. No. 514 - Tsai, B. and C. S. Gardner (December 1981), Remote Sensing of Sea State by Laser Altimeters.

RRL Rep. No. 518 - Gardner, C. S. (August 1982), Optical Communications.

RRL Rep. No. 519 - Im, K. E. and C. S. Gardner (September 1982), Atmospheric Effects on Baseline Error in Satellite Laser Ranging Systems.

RRL Rep. No. 526 - Im, K. E., B. M. Tsai and C. S. Gardner (September 1983), Analysis of Short Pulse Laser Altimetry Data Obtained over Horizontal Path.

RRL Rep. No. 527 - Tsai, B. M. and C. S. Gardner (March 1984), Theoretical and Experimental Analysis of Laser Altimeters for Barometric Measurements Over the Ocean.

EOSL Rep. No. 84-001 - Lafaw, D. A. and C. S. Gardner (August 1984), Timing Performance of Phase-Locked Loops in Optical Pulse Position Modulation Communication Systems.

EOSL Rep. No. 85-002 - Im, K. E. and C. S. Gardner (April 1985), Estimation of the Differential Pulse Propagation Times in Two-Color Laser Ranging Systems.

EOSL Rep. No. 85-003 - Chen, C. C. and C. S. Gardner (May 1985), Phase-Locked Loop Synchronization for Direct Detection Optical PPM Communication Systems.

EOSL Rep. No. 85-006 - Im, K. E. and C. S. Gardner (August 1985), Theoretical and Experimental Analysis of the Performance of Two-Color Laser Ranging Systems.

EOSL Rep. No. 85-009 - Gardner, C. S. (September 1985), Lidar Measurements of the Mesospheric Sodium Layer at the Air Force Geophysics Laboratory.

EOSL Rep. No. 87-002 - Chen, C. C. and C. S. Gardner (March 1987), Comparison of Direct and Heterodyne Detection Optical Intersatellite Communication Links.

EOSL Rep. No. 87-003 - Natarajan, S. and C. S. Gardner (May 1987), Phase Error Statistics of a Phase-Locked Loop Synchronized Direct Detection Optical PPM Communication System.

EOSL Rep. No. 87-004 - G. Hugh Song and C. S. Gardner (June 1987), Single-Color Laser Ranging with a Cube-Corner-Retroreflector Array.

EOSL Rep. No. 87-007 - Ball, C. K. (December 1987), Evaluation of a Satellite Laser Ranging Technique Using Pseudonoise Code Modulated Laser Diodes.

EOSL Rep. No. 87-008 - Miller, M. S., C. S. Gardner and C. H. Liu (December 1987), Raleigh Lidar Observations of Gravity Wave Activity in the stratosphere and lower mesosphere.

PAPERS PUBLISHED

C. S. Gardner, "Effects of Random Path Fluctuations on the Accuracy of Laser Ranging Data," Applied Optics, 15, 2539-2545, October 1976.

C. S. Gardner, "Effects of Horizontal Refractivity Gradients on the Accuracy of Laser Ranging to Satellites," Radio Science, 11, 1037-1044, December 1976.

C. S. Gardner, "Correction of Laser Tracking Data for the Effects of Horizontal Refractivity Gradients," Applied Optics, 16, 2427-2432, September 1977.

C. S. Gardner, R. Rowlett and B. E. Hendrickson, "Ray Tracing Evaluation of a Technique for Correcting the Refraction Errors in Satellite Tracking Data," Applied Optics, 17, 3143-3145, October 1978.

C. S. Gardner, "Technique for Remotely Measuring Surface Pressure from a Satellite Using a Multicolor Laser Ranging System," Applied Optics, 18, 3184-3189, September 1979.

C. S. Gardner, "Target Signatures for Laser Altimeters: An Analysis," Applied Optics, 21, 448-453, February 1982.

B. M. Tsai and C. S. Gardner, "Remote Sensing of Sea State Using Laser Altimeters," Applied Optics, 21, 3932-3940, November 1982.

C. S. Gardner, B. M. Tsai and J. B. Abshire, "Remote Sensing of Atmospheric Pressure and Sea State from Satellites Using Short-Pulse Multicolor Laser Altimeters," Proceedings of NATO-AGARD Symposium on Propagation Factors Affecting Remote Sensing by Radio Waves, 345, (46-1)-(46-11), Oberammergau, FRG, May 24-28, 1983.

C. S. Gardner, B. M. Tsai and K. E. Im, "Multicolor Laser Altimeters for Barometric Measurements over the Ocean: Theoretical," Applied Optics, 22, 2571-2577, September 1, 1983.

C. S. Gardner and J. B. Abshire, "Atmospheric refraction and target speckle effects on the accuracy of laser ranging systems," Proc. Int. Conf. on Laser Ranging Instrumentation, 1, 29-41, Royal Greenwich Observatory, Hearstmonceux, UK, September 24-28, 1984 (invited paper).

B. M. Tsai and C. S. Gardner, "Time-Resolved Speckle Effects on the Estimation of Laser Pulse Arrival Times," J. Opt. Soc. Amer. A., 2, 649-656, May 1985.

J. B. Abshire and C. S. Gardner, "Atmospheric Refractivity Corrections for Satellite Laser Ranging," IEEE Trans. Geosci. Remote Sensing, GE-2, 414-425, July 1985.

C. S. Gardner, "Remote Sensing of Atmospheric Pressure and Sea State Using Laser Altimetry," Proc. 1985 Int. Geosci. Remote Sensing Symps., 1, 199-206, Amherst, MA, October 7-9, 1985.

K. E. Im and C. S. Gardner, "Estimation of Differential Pulse Propagation Times in Two-Color Laser Ranging Systems," J. Opt. Soc. Amer. A., 3, 143-156, Jan. 1986.

C. C. Chen and C. S. Gardner, "Performance of Phase Locked Loop Synchronized Optical PPM Communication Systems," IEEE Trans. Comm., COM-34, 988-994, Oct. 1986.

C. S. Gardner, D. G. Voelz, C. R. Philbrick and D. P. Sipler, "Simultaneous lidar measurements of the sodium layer structure at the Air Force Geophysics Laboratory and the University of Illinois," J. Geophys. Res., 91, 12131-12136, November 1, 1986.

C. C. Chen and C. S. Gardner, "Loss Factors Associated with Spatial and Temporal Tracking Error in Intersatellite PPM Communication Links," Proc. IEEE Global Telescom Conf., 3, 1392-1397, Houston, TX, Dec. 1-4, 1986.

K. E. Im, C. S. Gardner, J. B. Abshire and J. F. McGarry, "Experimental evaluation of the performance of pulsed two-color laser ranging systems," J. Opt. Soc. Amer. A., 4, 820-833, May 1987.

C. C. Chen and C. S. Gardner, "Impact of Random Pointing and Tracking Errors on the Design of Coherent and Incoherent Optical Intersatellite Communication Links," IEEE Trans. Comm., to be published, 1987.